Advanced Devices & Instrumentation
A SCIENCE PARTNER JOURNAL

REVIEW ARTICLE

# Biomimetic Curved Artificial Compound Eyes: A Review

**Heng Jiang[1,2], Chi Chung Tsoi[1,2], Lanrui Sun[1,2], Weixing Yu[3], Hao Fan[3], Mengchao Ma[4], Yanwei Jia[5], and Xuming Zhang[1,2*]**

[1]Department of Applied Physics, The Hong Kong Polytechnic University, Hong Kong, China. [2]Photonics Research Institute, The Hong Kong Polytechnic University, Hong Kong, China. [3]Key Laboratory of Spectral Imaging Technology, Xi'an Institute of Optics and Precision Mechanics, Chinese Academy of Sciences, Xi'an, China. [4]Anhui Province Key Laboratory of Measuring Theory and Precision Instrument, School of Instrument Science and Opto-Electronics Engineering, Hefei University of Technology, Hefei, China. [5]State Key Laboratory of Analog and Mixed Signal VLSI, Institute of Microelectronics, University of Macau, Macau, China.

*Address correspondence to: apzhang@polyu.edu.hk

**Citation:** Jiang H, Tsoi CC, Sun L, Yu W, Fan H, Ma M, Jia Y, Zhang X. Biomimetic Curved Artificial Compound Eyes: A Review. *Adv. Devices Instrum.* 2024;5:Article 0034. https://doi.org/10.34133/adi.0034

Submitted 4 November 2023
Accepted 4 January 2024
Published 1 March 2024



Natural compound eyes (NCEs) are the most abundant and successful eye designs in the animal kingdom. An NCE consists of a number of ommatidia, which are distributed along a curved surface to receive light. This curved feature is critical to the functions of NCE, and it ensures that different ommatidia point to slightly different directions and thus enables panoramic vision, depth perception, and efficient motion tracking while minimizing aberration. Consequently, biomimetic curved artificial compound eyes (BCACEs) have garnered substantial research attention in replicating the anatomical configuration of their natural counterparts by distributing ommatidia across a curved surface. The reported BCACEs could be briefly categorized into 2 groups: fixed focal lengths and tunable focal lengths. The former could be further subcategorized into simplified BCACEs, BCACEs with photodetector arrays within curved surfaces, and BCACEs with light guides. The latter encompasses other tuning techniques such as fluidic pressure modulation, thermal effects, and pH adjustments. This work starts with a simple classification of NCEs and then provides a comprehensive review of main parameters, operational mechanisms, recent advancements, fabrication methodologies, and potential applications of BCACEs. Finally, discussions are provided on future research and development. Compared with other available review articles on artificial compound eyes, our work is distinctive since we focus especially on the "curved" ones, which are difficult to fabricate but closely resemble the architecture and functions of NCEs, and could potentially revolutionize the imaging systems in surveillance, machine vision, and unmanned vehicles.

## Introduction

In 1664, Hooke et al. [1] discovered that the cornea of a gray drone fly, in which pearls (i.e., corneal facet lenses) were orderly arranged, was fundamentally different from that of a human being. This discovery marked the beginning of the observation and research of natural compound eyes (NCEs). Two centuries later, another renowned biologist, Exner [2], proposed the concept of the basic unit of an NCE, which was so-called the ommatidium. A typical ommatidium collects light at a specific angle through a corneal facet lens and then conveys it to the photoreceptor cells via a crystalline cone and a rhabdom (light guide) (see Fig. 1A). Axon bundles subsequently innervate ommatidia through synaptic connections in lamina cartridges. Deeper neural centers (medulla and lobula) process the primary signals before transmitting the information to the central brain (see Fig. 1B).

The NCEs have several types of anatomical structures [3] as illustrated in Fig. 1B to D (to be elaborated in the "Classification of NCEs" section), which are very different from other types of eyes [4]. The NCEs offer substantial advantages, including wide field of view (FOV), exceptional motion detection sensitivity, and an infinite depth of field. Specifically, wide FOV is easy to understand on the basis of Fig. 1. The exceptional motion detection sensitivity can be attributed to 2 key factors. First, the miniature vision of NCEs markedly diminishes the signal transmission distance between the photoreceptor and the brain. Second, NCEs exhibit a nonspiking graded signal transmission rate between the retina and lamina neurons ($1{,}650\ \mathrm{bit{\cdot}s^{-1}}$), surpassing that of human spiking neurons ($\sim 300\ \mathrm{bit{\cdot}s^{-1}}$). This discrepancy arises from the presence of a refractory period in spiking neurons, imposing constraints on the speed of information transmission [5,6]. The infinite depth of field is a result of the low acceptance angle of each ommatidium, causing incident light to approach near parallelism. Artificial compound eyes (ACEs) that replicate NCEs can also harness these benefits. Consequently, they have found niche applications in various micro-optics fields such as microcameras

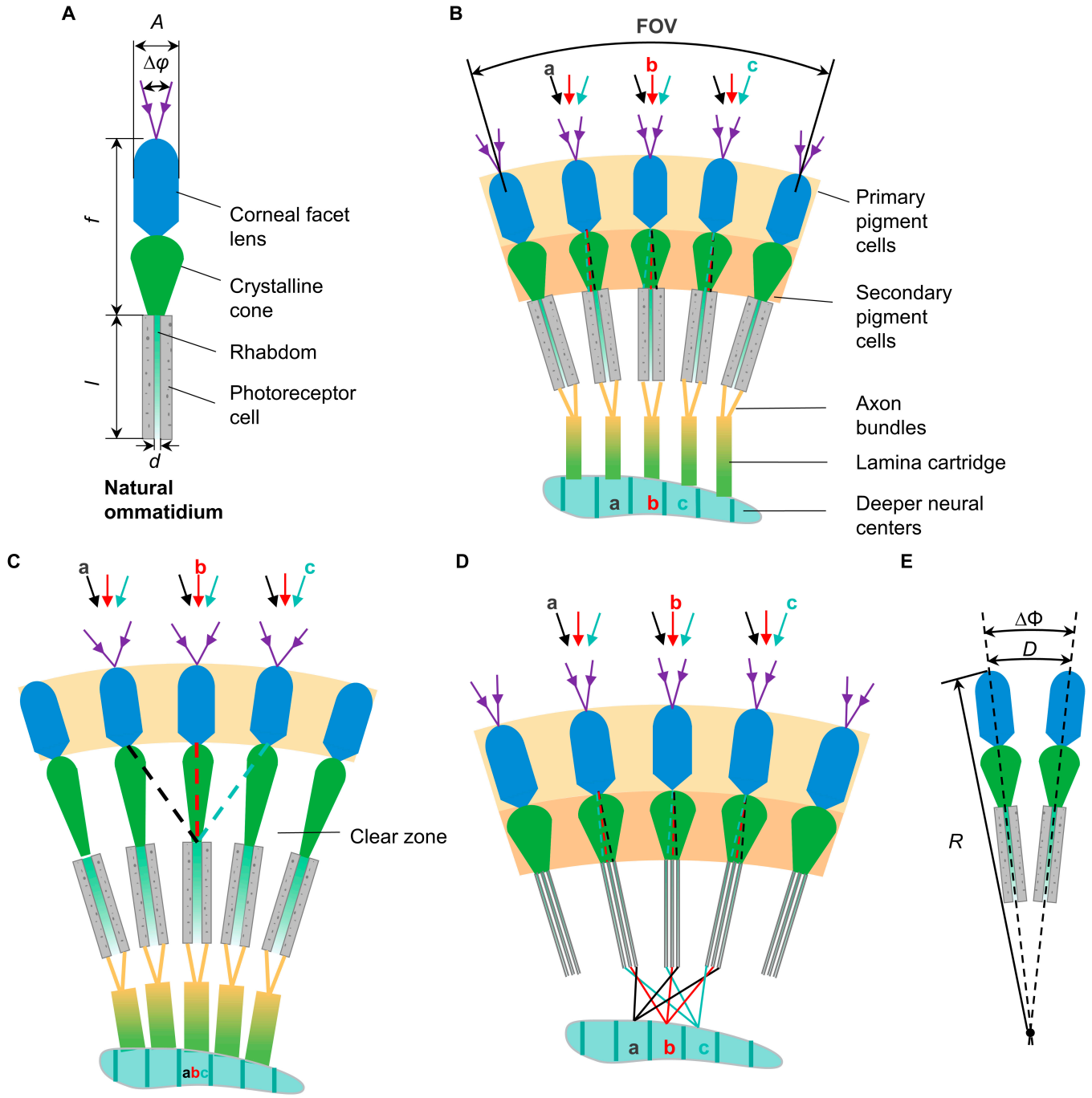


**Fig. 1.** Schematic diagrams of NCEs. (A) Natural ommatidium. (B) Apposition NCE. (C) Optic superposition NCE. (D) Neural superposition NCE. (E) Interpretation for interommatidial angle.

[7], medical imaging [8], and elementary motion detectors [9]. Noteworthily, ACEs and artificial retinas are truly mirror concepts, with the former mimicking the NCEs of arthropods for panoramic perception and high-speed dynamic motion detection, while the latter emulates the retinas of vertebrates' eyes to assist in the improvement of visual loss in the fields of medicine and bioengineering [10].

ACEs can be generally divided into 3 categories: planar microlens arrays, ACEs using metalenses, and biomimetic curved ACEs (BCACEs). With regard to the first one, all microlenses are arranged in a plane to replace a single lens with higher resolution and variable focal lengths. A few reviews have covered the progress and implementation of planar microlens arrays [11–15]. Nussbaum gave a comprehensive discussion of the planar ones on their designs and fabrications [11], emphasizing properties of plano-convex microlens arrays (e.g., radius of curvature, focal length, and packing density), fabrication techniques (e.g., reflow method and reactive ion etching), testing methods, and potential applications. On this basis, some planar microlenses were proposed with fixed and tunable focal lengths [12,15]. For example, Brückner et al. [12] reported an approach to stitching the partial images recorded by planar

microlenses to compose a conclusive image of the entire FOV. Similarly, Tanida et al. [13] and Shankar et al. [14] presented their designs with ultrathin multiple channels. In addition, Ren and Wu [15] reported a dielectrophoresis-based tunable-focus liquid microlens array. However, the planar microlens arrays usually have very limited FOV; therefore, this type will not be discussed further.

Metalenses consist of a 2-dimensional (2D) array of subwavelength scatterers that manipulate wavefronts, inducing abrupt phase changes at the interface. Through the precise design of the geometrical nanoparameters of these scatters, incident light from various directions is efficiently scattered into the substrate via discrete nanobuilding blocks, generating photocurrents [16–19]. The utilization of metalenses in the design of ACEs represents an emerging approach, pointing toward a promising future. When compared to traditional BCACEs, ACEs incorporating metalenses exhibit several merits, such as an FOV (e.g., 170° [16]) comparable to that of most BCACEs, a more compact design, and the potential to overcome chromatic aberration effects [17]. However, this type of ACE also encounters certain limitations. For example, its focusing efficiency at the edge is much lower than at the center (e.g., 45% at an incident of 85° compared to 82% at a normal incident [16]); it is challenging for metalens-based ACEs to achieve or surpass an FOV of 180°, which may be more feasible for BCACEs. It is important to note that while an ACE utilizing metalenses operates by amalgamating separate light information from a wide FOV like an NCE, its underlying specific working principle deviates markedly from that of an NCE. Therefore, it is pertinent to mention that the details of this deviation from NCE principles are beyond the scope of this paper.

Regarding BCACEs, the fundamental structural unit is the artificial ommatidium, comprising several key components: the microlens (dispersed across a curved surface to ensure perpendicularity to panoramic light), a cone with dielectric properties (mimicking the crystalline cone in nature to facilitate the guidance of focused light from the microlens into the light guide core), the light guide core (analogous to the rhabdom found in nature), light guide cladding, and the photodetector, as shown in Fig. 2A. Therefore, BCACEs possess a broad FOV, minimal geometric aberration (although other aberrations such as chromatic aberration and astigmatism may still remain), exceptional optical uniformity, resolution, and sensitivity, rendering them suitable for a broader spectrum of applications.

The investigation of BCACEs experienced a tortuous process. Figure 3 summarizes the categories of BCACEs. According to the reported designs of BCACEs, 2 types exist: ones with

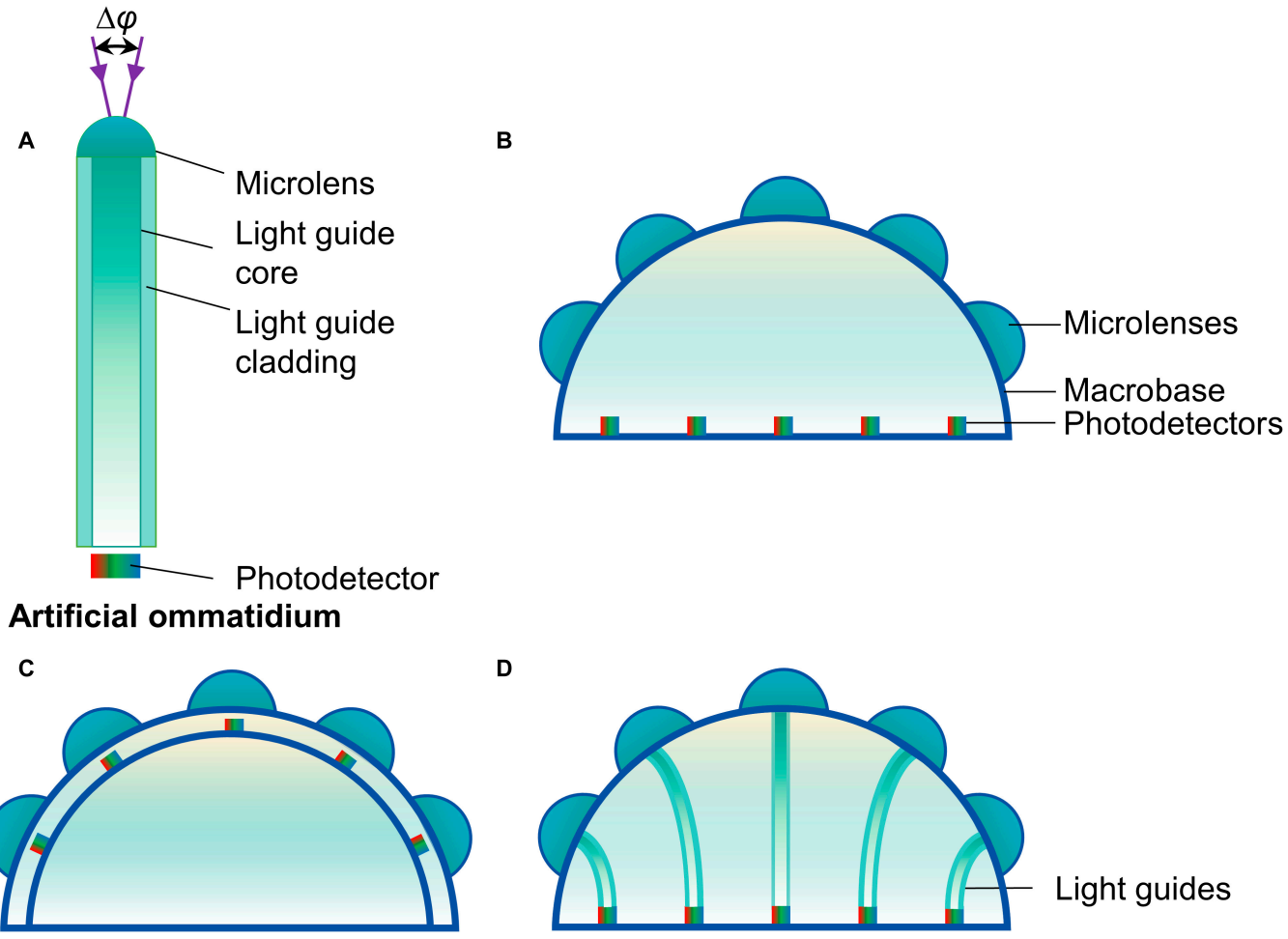


**Fig. 2.** Schematic diagrams of BCACEs. (A) Artificial ommatidium. (B) Simplified BCACE. (C) BCACE with a photodetector array within a curved surface. (D) BCACE with light guides.

fixed focal lengths and ones with tunable focal lengths, meaning that the focal length of the former's microlens array is fixed, while the latter's microlens can be altered. In the case of fixed focal length BCACEs, some research was devoted to designing and optimizing simplified BCACEs [20–23]. The reason to call this kind of BCACEs simplified BCACEs is that they are typically composed of a curved macrobase and a microlens array (not completed ommatidia; Fig. 2B). Because of the imperfection, it is difficult to ensure that the light from each microlens focuses on the same detection plane, especially when the number of microlenses is large. Therefore, some researchers proposed BCACEs with photodetector arrays within curved surfaces as shown in Fig. 2C [24–28]. Although it is promising to use a photodetector array within a curved surface to record the light information from the curved microlens array, it still suffers hard fabrication and reproduction. In this way, some researchers proposed the BCACEs with light guides as shown in Fig. 2D [29–35]. With the help of light guides, the photodetector array within a curved surface can be replaced by the planar photodetector array, increasing the robustness of the BCACEs. Besides, such BCACEs are more similar to NCEs in anatomic structures.

In the case of tunable focal length BCACEs, they can be classified into distinct groups depending on the techniques utilized to alter the shapes of microlenses to finally modify the focal lengths, for example, fluidic pressure [36,37], thermal effect [38,39], and pH [40].

This article is divided into 8 sections. The initial section introduces the concept of BCACEs. In the subsequent section ("Classification of NCEs" section), we offer an in-depth exploration of NCEs. Moving on to third section, we propose several parameters for evaluating BCACEs. The fourth section provides a detailed discussion of BCACEs, focusing on their operational mechanisms. Moving on to the fifth section, we present various fabrication methods for BCACEs. In addition, the sixth section showcases some applications, followed by a brief discussion in the seventh section. Finally, we conclude the article in the last section.

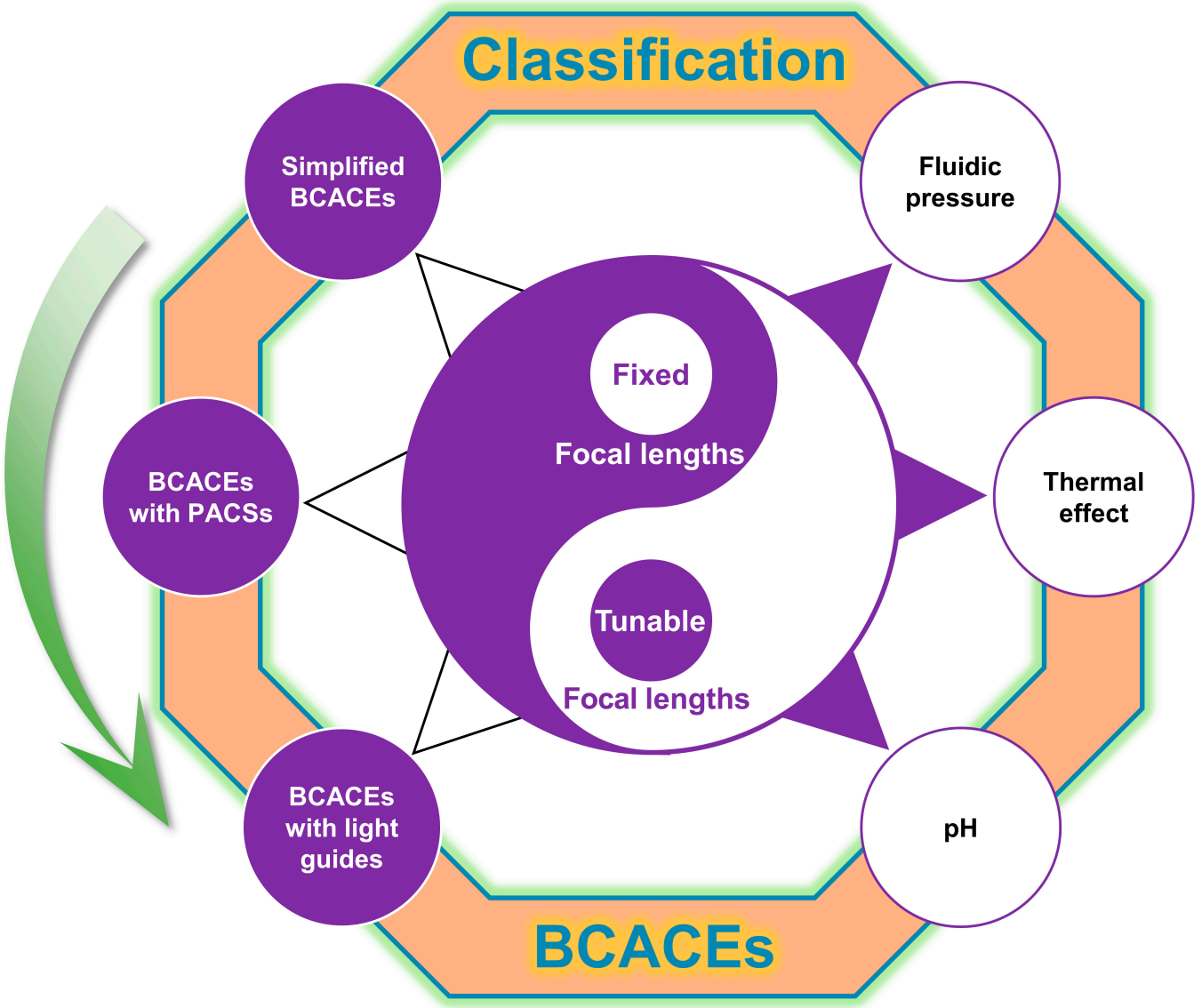


**Fig. 3.** Category of BCACEs. PACSs, photodetector arrays within curved surfaces.

## Classification of NCEs

NCEs can be specifically classified into 3 distinct types: apposition NCEs, optic superposition NCEs, and neuron superposition NCEs [41]. Apposition NCEs typically arrange ommatidia along a curved surface and separate them with pigment cells (see Fig. 1B). Because of the small diameter of the rhabdom and the presence of pigment cells, the light information from each ommatidium can only be focused on its corresponding rhabdom and transmitted to the corresponding deeper neural center. Consequently, the acceptance angle of each ommatidium is limited (approximately 1° for bees [42,43]), resulting in high resolution. However, this limited acceptance angle also leads to low optical sensitivity. Therefore, such NCEs are typically found in diurnal insect eyes.

Optic superposition NCEs are similar to the apposition type during the day, apart from a longer crystalline tract in the clear zone (see Fig. 1C) and a larger rhabdom diameter. This larger rhabdom diameter results in a broader acceptance angle for optic superposition NCEs (e.g., 19° for moths during the day; data sourced from [44,45]). While the increased acceptance angle reduces imaging resolution, it enhances sensitivity to light. When dim light is present, pigment migration causes light from neighboring microlenses to converge onto one rhabdom through the clear zone [46–48], further increasing the optical level in one rhabdom. Therefore, such NCEs are better suited for insects adapted to nocturnal life and low-light conditions [41].

In contrast to the previously mentioned NCEs with fused rhabdoms, neural superposition NCEs feature separate rhabdomeres, each receiving light input from different visual axes, representing different points in the environment (see Fig. 1D). Axons from each individual rhabdomere transport light input originating from the identical visual axis but emerging from separate ommatidia, ultimately converging into a shared lamina cartridge [41]. This configuration allows for both high resolution and high optical sensitivity at the cost of complex anatomical structures.

## Characteristics of BCACEs

The evaluation of BCACEs in this section focuses on 2 key merits: panoramic imaging and high sensitivity to motion. In terms of the former, we consider factors such as FOV, acceptance angle of each ommatidium, interommatidial angle, imaging quality, and optical sensitivity. Regarding the latter, the emphasis is on illustrating the highest angular perception speed.

### Field of view

The concept of FOV originates from NCEs, as illustrated in Fig. 1B. It represents the collective acceptance angle of compound eyes and serves as a crucial parameter to showcase the panoramic imaging and dynamic motion detection capabilities of BCACEs.

### Acceptance angle of each ommatidium

The acceptance angle of each ommatidium, denoted as $\Delta\varphi = d/f$, is also derived from NCEs [24,42]. Here, $d$ represents the rhabdom diameter, while $f$ signifies the focal length of the facet lens (see Fig. 1A). In some assays [25,34], the full width at half maximum (FWHM) of the angular sensitivity function is roughly to be seen as the acceptance angle. This parameter serves as a critical element in determining the resolution and optical sensitivity of the compound eye.

### Interommatidial angle

The interommatidial angle, denoted as $\Delta\Phi = D/R$, is defined as the angular separation between 2 neighboring ommatidia. Here, $D$ represents the arc distance between neighboring ommatidia, while $R$ signifies the local radius of curvature. Typically, this parameter is either equal to or slightly larger than $\Delta\varphi$ for apposition compound eyes. This is because if $\Delta\Phi$ were much larger than $\Delta\varphi$, there would be a significant gap between neighboring ommatidia, resulting in a loss of light information. Conversely, if $\Delta\Phi$ were smaller than $\Delta\varphi$, there would be substantial overlap between neighboring ommatidia, leading to a reduction in resolution. While this parameter is derived from NCEs [42], as shown in Fig. 1E, it can also be applied to evaluate BCACEs using the same definition.

### Quantitative imaging performance metric

The modulation transfer function (MTF) serves as a ubiquitous parameter used for evaluating the imaging quality of an optical system. It represents the system's ability to transfer input modulation to output modulation. Typically, MTF is calculated by dividing the output contrast by the input contrast, with contrast $C$ defined as:

$$C = \frac{I_{\max} - I_{\min}}{I_{\max} + I_{\min}}, \tag{1}$$

where $I_{\max}$ and $I_{\min}$ represent the maximum and minimum intensities of the object, respectively. In addition, MTF is graphically represented with the $x$ axis representing spatial frequency (light pairs per micrometer, lp mm$^{-1}$) and the $y$ axis representing MTF. MTF serves as a crucial parameter for evaluating the imaging quality of BCACEs. However, it is important to note that BCACEs in their current stage exhibit poor imaging quality, to the extent that they cannot even be effectively assessed using MTF. Looking ahead, as BCACEs continue to undergo rapid development and improvements in imaging quality, MTF can become a genuinely valuable tool for their evaluation.

### Optical sensitivity

The term optical sensitivity $S$ describes the light-gathering abilities of compound eyes under varying light intensities. When dealing with a broad-spectrum light source, $S$ behaves as follows,

$$S = \left(\frac{\pi}{4}\right)^2 A^2 \left(\frac{d}{f}\right)^2 \left(\frac{kl}{2.3 + kl}\right), \tag{2}$$

and if the light source is monochromatic, $S$ follows

$$S = \left(\frac{\pi}{4}\right)^2 A^2 \left(\frac{d}{f}\right)^2 \left(1 - e^{-kl}\right), \tag{3}$$

where $A$, $d$, $f$, $k$, and $l$ denote the diameter of the compound eye's aperture, the diameter of the rhabdom, the focal length, the absorption coefficient of the photoreceptor cells on the rhabdom, and the length of the rhabdom, respectively (see Fig. 1A) [49]. In both equations, $(\pi/4)^2 A^2$ accounts for the sectional dimension of the ommatidium, $\left(\frac{d}{f}\right)$ is the acceptance angle of

the ommatidium, and $kl/(2.3 + kl)$ and $(1 - e^{-kl})$ represent the light absorption abilities. Therefore, the optical sensitivity $S$ is subject to the size, the acceptance angle, and the light absorption ability of ommatidia. In a similar matter, this nature-inspired parameter can be used for the evaluation of BCACEs.

### Highest angular perception speed

If one BCACE is used to track an object moving from one side of the BCACE to the opposite side, the time $\Delta t$ can be determined as follows:

$$\Delta t = \frac{\mathrm{FOV}}{\omega}, \tag{4}$$

where $\omega$ symbolizes the angular speed. Each BCACE has the lowest detection interval time $\Delta t_{\mathrm{dec}}$. For example, if the photodetector of the BCACE is a complementary metal-oxide semiconductor (CMOS) chip, $\Delta t_{\mathrm{dec}}$ is determined by the frame rate of the CMOS. Obviously, $\Delta t$ should not be smaller than $\Delta t_{\mathrm{dec}}$, i.e.,

$$\Delta t \geq \Delta t_{dec}, \tag{5}$$

and thus,

$$\frac{\mathrm{FOV}}{\omega} \geq \Delta t_{dec}. \tag{6}$$

Here, the highest angular perception speed can be expressed as

$$\omega_{\max} = \frac{\mathrm{FOV}}{\Delta t_{dec}}. \tag{7}$$

## Classification of BCACEs

Within this section, the discussion will delve further into BCACEs, specifically exploring their operational mechanisms. First, we will introduce 3 types of BCACEs with fixed focal lengths. Subsequently, various methods for altering the focal lengths of BCACEs will be discussed. A general comparison of representative BCACEs is provided in Table.

### BCACEs with fixed focal lengths

#### *Research on simplified BCACEs*

During the initial stage of the research, researchers were devoted to the layout of microlenses in an ordered manner (compactness had not yet been deliberated). For example, as shown in Fig. 4A, Li's group [20,50,51] suggested dividing the curved surface of the BCACE into 3 equal sections, each spanning an angle of 120° (distinguished by different colors: red, yellow, and green), with each section having a distinct focal length, ultimately enabling limited zoom capability. To ensure that all microlenses on the curved surface effectively converge light onto a planar photodetector array, microlenses in each segment are categorized into 5 tiers based on their deviation angle concerning the central microlens, as shown in Fig. 4B.

The effective focal lengths of microlenses at all tiers can be determined through the thin lens manufacturing equation:

$$\frac{1}{f_n} = (n_i - 1)\left(\frac{1}{r_n} - \frac{1}{R}\right), \tag{8}$$

where $f_n$ represents the effective focal length of the $n$th microlens, $r_n$ denotes the radius of curvature of the $n$th microlens, $R$ signifies the radius of the curved surface base, and $n_i$ stands for the refractive index of the material used for this simplified BCACE. By using this formula, the effective radii of microlenses can be estimated, and then all microlenses can be designed by using Zemax to focus onto a planar photodetector array. However, as the number of microlenses increases, this method becomes increasingly challenging because of the inherent design drawbacks and the complexity involved in both design and fabrication.

Furthermore, Lian's team [23] developed a simplified form of BCACE (Fig. 4C) in an effort to enhance compactness. However, Lian's design has an inverted light path compared to Li's design, where light passes through the microlenses on the curved surface and focuses onto a plane as shown in Fig. 4D. It follows an optical path from one point or plane to another, without directly addressing the intricate light propagation from the curved surface to a plane.

Moreover, the round lens shape and fill factor (the ratio of the area that directs light to the photosensor, to the total contiguous area occupied by the microlens array, approximately 50% to 70%) of the aforementioned BCACE are markedly distinct from those found in natural ones, leading to a considerable impact on the signal-to-noise ratio. In this way, Wu's laboratory [21] optimized the shape of the microlens as a hexagon to achieve a 100% fill factor so as to achieve a favorable light signal-to-noise ratio as depicted in Fig. 4E and F. To assess the optical performance of this design quantitatively, they measured the point spread functions (PSFs) along the $x$ and $y$ axes, as illustrated in Fig. 4G and H. These measurements were then compared with those of a single reference lens, depicted in Fig. 4I and J. The results show that the FWHM of this BCACE remains stable, even when exposed to tilted incident light, while the FWHM of a single lens increases dramatically, showing that the imaging distortion of Wu's design is tiny.

Similarly, Jin's team also fabricated hexagonal-shaped compound eyes with different numbers of microlenses as shown in Fig. 4K and L, showing that the hexagonal shape had a high optical imaging uniformity [22].

Here, simplified BCACEs primarily concentrate on the microlenses situated on the curved surface. Despite the principal role of microlenses within the compound eye, in-depth research into numerous other critical components is lacking, resulting in several inherent limitations. For example, the absence of pigment cells leads to severe cross-talk between neighboring ommatidia. Similarly, despite certain endeavors being made to direct the light from microlenses onto a focal plane, due to the absence of effective light guides, it is an obvious challenge to design and fabricate this kind of compound eye with satisfactory FOV and image resolution. Correspondingly, BCACEs with photodetector arrays within curved surfaces and BCACEs with light guides attempt to address these challenges.

#### *Research on BCACEs with photodetector arrays within curved surfaces*

Since a solo microlens array component was unable to effectively focus light onto a common planar photodetector as the number of microlenses increased, researchers thus explored the possibility of replacing the planar photodetector array with a curved one. By ensuring a proper spatial relationship between each microlens and photodetector, it is possible for the microlens to successfully focus light onto its corresponding photodetector. Regarding this kind of BCACE, some researchers focused on

**Table.** Comparison of typical BCACEs

| Type of BCACE | Numbers of ommatidia | Shape of microlenses | BCACE radius | FOV (Maximum) | Materials | Fabrication methods | References |
|---|---|---|---|---|---|---|---|
| **Ones with fixed focal lengths** | | | | | | | |
| Simplified BCACEs | 61 | Round | 4.33 mm | 48° | PDMS | – | [20] |
| | – | Hexagon | 40 μm | 60° | SU-8 resin | Laser direct writing | [21] |
| | 19 | Hexagon | 45 μm | 120° | SU-8 resin and PDMS | Laser direct writing | [22] |
| | 581 | Round | – | 108° | PDMS, silicon, photoresist, etc. | Lithography, plasma etching, gas-assisted deformation, etc. | [23] |
| BCACEs with PACSs | 180 | Round | 6.96 mm | 160° | PDMS, silicon, silicone, etc. | Combine, stretch, etc. | [24] |
| | 630 | Round | 6.4 mm | 180° × 60° | Glass, printed circuit board, etc. | Dicing, bending, etc. | [25] |
| BCACEs with light guides | 8,370 | Hexagon | 1.25 mm | – | PDMS, silicon, photoresist, etc. | Lithography and gas-assisted deformation | [29] |
| | 522 | Hexagon | 2.5 mm | 170° | Acrylate resin, UV-curable diacrylate polymer, and silicone | Projection microstereolithography 3D printing and microfluidic-assisted moulding technique | [34] |
| **Ones with tunable focal lengths** | | | | | | | |
| Fluidic pressure | 100 | Round | 50 mm | – | PDMS | – | [36] |
| | 9 | Round | – | 120° | PDMS, SU-8 | Lithography | [37] |
| Thermal effect | ~900 | Round | – | 160° | Graphene | Template-directed self-assembly method | [38] |
| | 3 | Round | – | – | PDMS, *N*-isopropylacrylamide, etc. | Lithography | [39] |
| pH | –(tunable base)<br>7(fixed base) | Hexagon | 32 μm (tunable base)<br>50 μm (fixed base) | 80° | BSA protein and SU-8 resin | Laser direct writing | [40] |

constructing a system and testing its static characteristics [24], while others researched dynamic characteristics [25].

Specifically, Song et al. [24,26] proposed a type of BCACE inspired by the arthropod eye and tested it. As shown in Fig. 5A, the 2 major subsystems are combined to form the hemispherical apposition compound eyes, the top subsystem providing optical imaging function and defining the overall mechanics that comprises 180 effective microlenses and the bottom subsystem, responsible for photodetection and electrical readout, comprising a complementary array of photodiodes and blocking diodes [24]. Following a series of dimensional and material selections, each photodiode is positioned at the focal point of a corresponding microlens to create an integrated imaging system, as depicted in Fig. 5B. In consequence, both subsystems are combined and stretched from the planar layout to the hemispherical shape under the hydraulic actuation as shown in Fig. 5C. Furthermore, an upper perforated sheet and a lower bulk support (see Fig. 5E) are constructed from black silicone to minimize stray light. Here, the black silicone is made by mixing the carbon black powder (Strem Chemical) to a thin silicone film membrane (Ecoflex, smooth-on), which undergoes laser machining. In addition, there is a thin-film insert featuring metalized contact pads that connect to a printed circuit board, serving as an interface for external control electronics. These combined subsystems are bonded together to constitute the complete apposition compound eye, as depicted in Fig. 5D. Therefore, a BCACE is obtained, with the microlenses and the supporting posts as corneal lenses and crystalline cones,

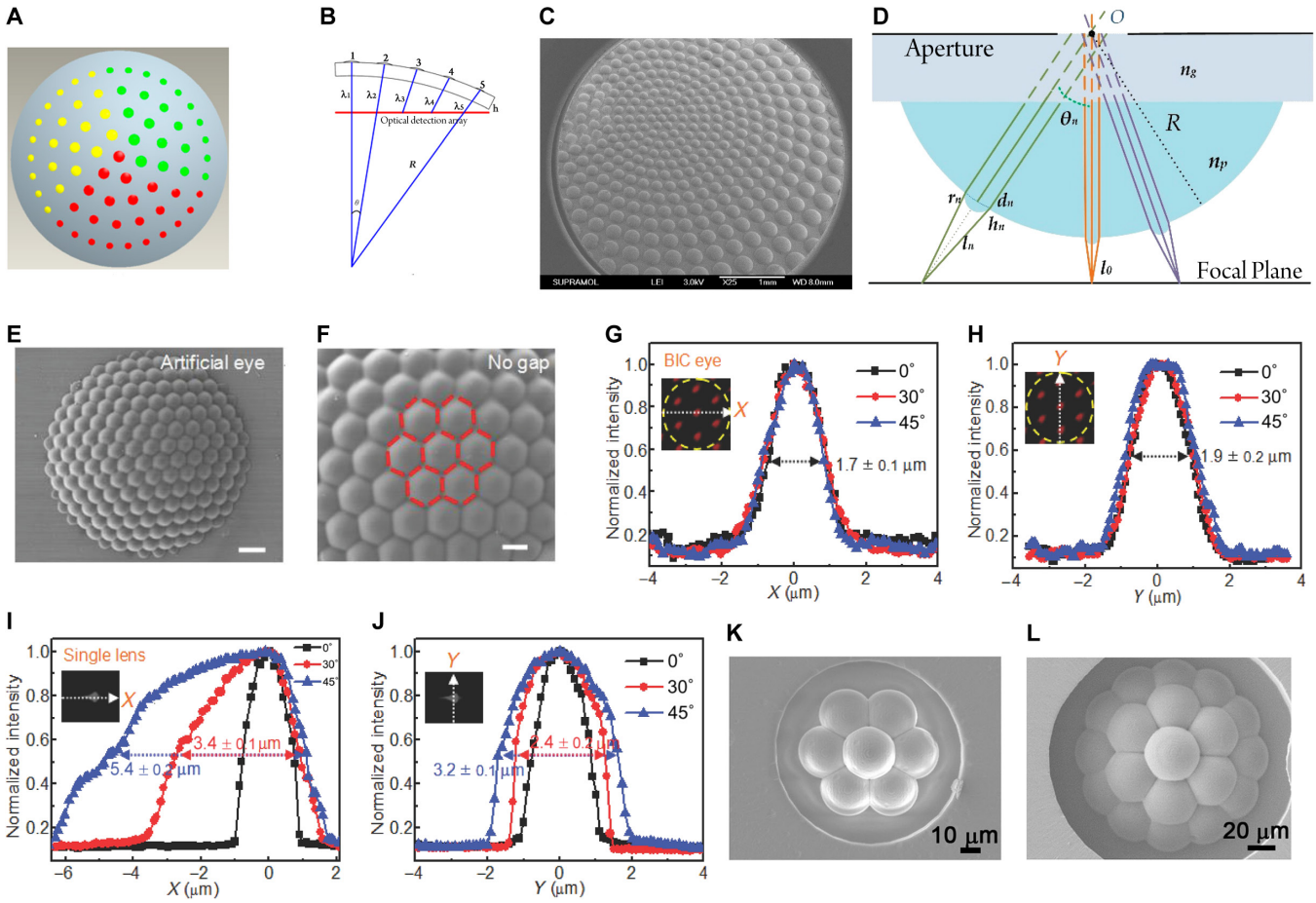


**Fig. 4.** Simplified BCACEs. (A) Area division of the variable focus surface compound eye proposed by Li's group, where the 3 different hues represented the 3 regions divided. (B) Positional relationship between microlenses and the focus planes at all levels: $R$, curved base radius; $\theta$, suborbital deflection angle; $\lambda_{1-5}$, distance between the microlenses and the optical detection array. Reprinted with permission from [20] © MDPI. (C) Scanning electron microscopy (SEM) image of Lian's BCACE at side view. (D) Light path design of Lian's BCACE. Reprinted with permission from [23] © MDPI. (E) Top-view SEM images of Wu's BCACE. (F) Thirty-degree tilted magnified SEM images of the BCACE and the 100% fill factor of hexagonal microlenses. Scale bars. 10 μm (E) and 5 μm (F). (G and I) Comparison of $x$-direction PSF for Wu's BCACE and single microlens. (H and J) $y$-direction PSF of Wu's BCACE and a single lens. The insets in (G) to (J) are the focus spots of Wu's BCACE and single microlens under 30° light incidence. BIC, biologically inspired compound. Reprinted with permission from [21] © John Wiley and Sons. (K and L) 3D images of Jin's BCACE with 7 microlenses (K) and 19 microlenses (L). Reprinted with permission from [22] © AIP Publishing.

respectively, and photodiodes as photoreceptors on the rhabdom, as compared with NCEs.

Some static experiments were thereby carried out. Since photodiodes are discrete, the scanning procedure is imperative for the ultimate formation of an image. In Fig. 5F, images of a line-art soccer ball illustration positioned at 3 distinct angular orientations: −50° (left), 0° (center), and 50° (right) demonstrate that this compound eye boasts the ability to scan images from various angles without anomalous blurring or aberrations. Quantitative analysis can be conducted by illuminating with a laser at angles varying from −80° to 80° in 20° increments, in both the $x$ and $y$ directions. This is demonstrated in a consolidated image shown in Fig. 5G, demonstrating that the FOV is 160°. Figure 5H and I illustrates that this compound eye can accurately and simultaneously render numerous objects situated at significantly diverse angular orientations and distances.

To further improve the FOV, this group endeavored to mimic the anatomical structure of a fiddler crab's compound eyes [27]. In this work, the author followed the herein-before research principle to precisely align each microlens and its corresponding photodetector on curved surfaces and used a black layer to prevent cross-talk. The major progress of this work lies in the expansion of FOV to a range of 160° vertically and 300° horizontally. Furthermore, the graded microlens closely mimics the flat corneal lens and the observed graded refractive index structure in the fiddler crab's eye. As a result, it exhibits few alterations in its focusing power when exposed to changes in the external medium. Consequently, this ACE is capable of producing clear amphibious images, even when objects are positioned at varying distances in the air.

In contradistinction to the research conducted by Song et al., which primarily concentrated on the static properties of BCACEs, Floreano et al. [25,28] exhibited a distinct emphasis on their dynamic characteristics. Figure 5J is the image of their prototype whose FOV is 180° × 60 as shown in Fig. 5K [25]. This prototype consists of 3 major layers: an optical layer, a photodetector layer, and a printed circuit board as shown in Fig. 5L. Specifically, the optical layer is constituted of an assemblage of exceptionally transparent polymer microlenses and 2 low-reflectivity opaque metal layers, each featuring corresponding pinhole patterns, the former focusing light precisely onto the photodetector layer, while the latter suppressing optical cross-talk. Besides, the

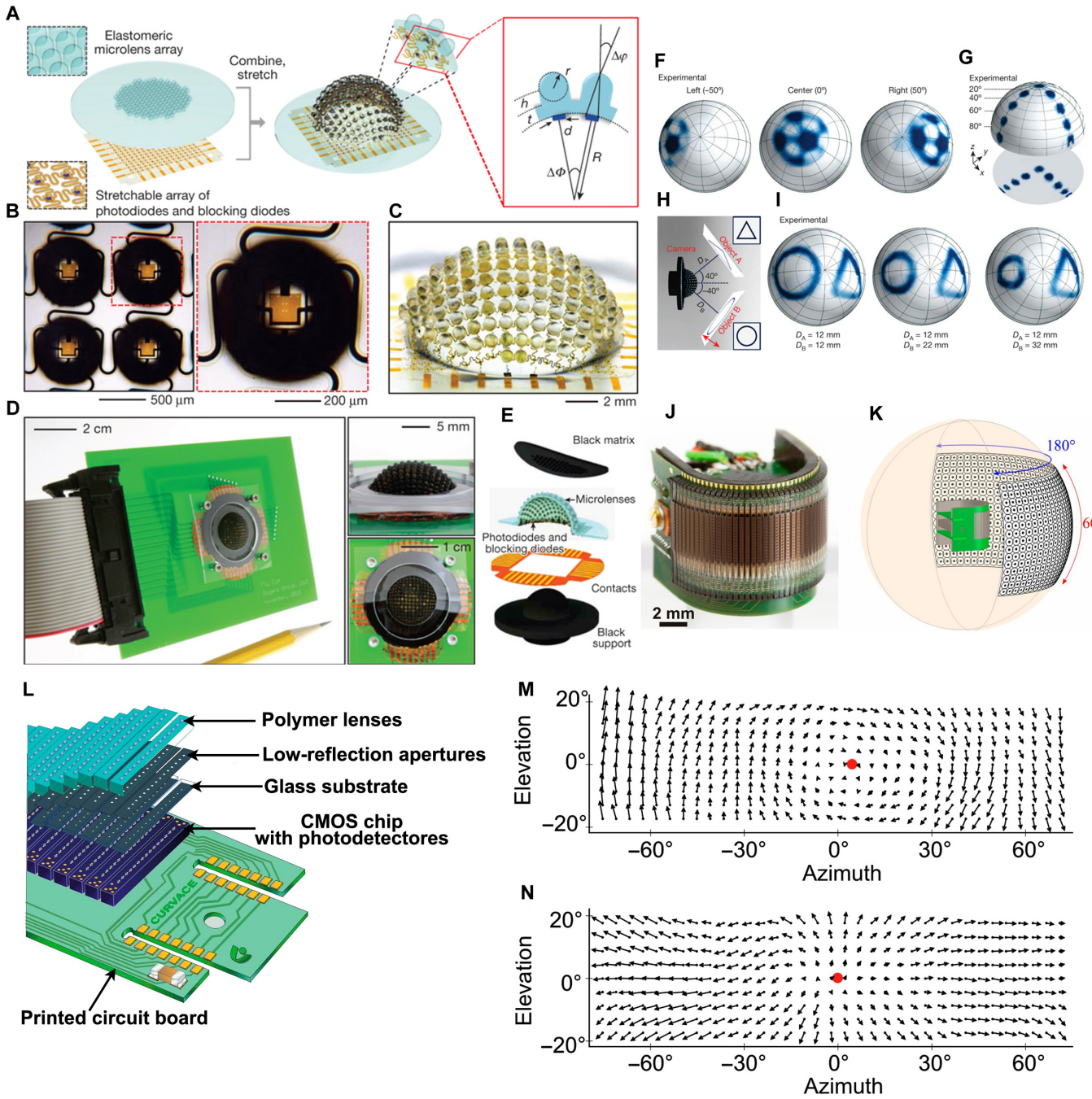


**Fig. 5.** BCACEs with photodetector arrays within curved surfaces. (A to I) BCACE proposed by Song's group. Reprinted with permission from [24] © Springer Nature. (A) Illustrations of an array of elastomeric microlenses and their supporting posts connected by a base membrane, as well as a corresponding array of silicon photodiodes and blocking diodes interconnected. (B) Optical micrograph of 4 adjacent ommatidia in a flat configuration (on the left), along with an enlarged view (on the right). (C) Image of a representative system after hemispherical deformation. (D) Photograph of a finished compound eye installed on a printed circuit board, serving as an interface to external control electronics (on the left), with close-up views in the insets. (E) Exploded-view illustration of these BCACE components. (F) Images of a soccer ball illustration taken from 3 distinct polar angles in relation to the camera's center. (G) Composite image displaying the sequential illumination of the compound eye using a collimated laser beam at 9 different angles of incidence, shown on a hemispherical surface (top) and projected onto a plane (bottom). (H) Schematic illustration of an experimental arrangement designed to illustrate essential imaging characteristics. One object (object A, marked as a triangle) is positioned at an angular location of 40° with a distance of $D_A$, while the other (object B, denoted as a circle) is at −40° with a distance of $D_B$. (I) Photographs of these objects captured at various $D_B$ values. (J to N) BCACE proposed by Floreano's group. Reprinted with permission from [25] © Proceedings of the National Academy of Sciences. (J) Image of the prototype. (K) Illustration of the panoramic FOV of the prototype. (L) Scheme of the 3 layers that compose this BCACE. (M and N) Dynamic optical flow detection involving the identification of a red dot as the center or focal point of motion. (M) Rolling motion toward a wall adorned with random black and white patterns. (N) Linear translation toward this wall.

photodetector layer aims to record the signal for subsequent processing, and the printed circuit board aims to collect and transmit the signals emitted from the ommatidia to the processing units.

Since photodetectors are discrete, the direct imaging result of this ACE is mosaic. Consequently, it is more appropriate to investigate its dynamic characteristics. For example, Fig.

5M and N illustrates the capability of this ACE to detect dynamic optical flow under various motion conditions.

In this section, the research on BCACEs evolves to incorporate a hybrid configuration of microlens arrays and photodetector arrays. This facilitates the recording of light information from a curved microlens array by replacing the conventional planar photodetector array with a photodetector array within a curved surface. However, there are also several limitations associated with this approach. First, the fabrication and reproduction of the photodetector array within a curved surface are challenging because of the distribution of photodetectors on a curved surface. Second, the presence of interspaces between photodetectors hinders the ACE from fulfilling the requirements of both static imaging and dynamic motion detection. This is due to the need for a scanning procedure to achieve static imaging, which ultimately reduces the imaging rate significantly. Consequently, dynamic motion detection relies on direct imaging, and the mosaic images cannot be avoided. Third, while this ACE design bears a greater resemblance to NCEs compared to previous versions that only incorporate microlenses, it still lacks certain components found in NCEs, such as light guides.

### *Research on BCACEs with light guides*

Similar to NCEs, BCACEs discussed in this section harness light guides to transmit light information from microlenses to photodetectors. The incorporation of light guides eliminates the necessity for arranging photodetectors along a curved surface. This modification leads to a reduction in the design and fabrication complexity of photodetector arrays within curved surfaces and an enhancement in the efficiency of light transmission.

Such particular ACE designs are rooted in the work of Jeong et al. [29]. In their study, Jeong proposed the use of the disparity in refractive indices between the light guide core and the light guide cladding (or waveguide core and waveguide cladding, as presented in this paper) to mimic the function of the rhabdom found in natural ommatidia, serving as the light guide, as illustrated in Fig. 6A. Both the light guide core and cladding in this instance are fabricated from SU-8 material. The distinction lies in the fact that the SU-8 material used for the core undergoes ultraviolet (UV) exposure, whereas the SU-8 material for the cladding does not. This differential treatment results in a final refractive index difference with a value of 0.029.

While Jeong's initial proposal aimed to use a light guide for transmitting optical information from a curved microlens array to a planar surface, he encountered limitations in achieving both static imaging and dynamic motion detection. This challenge stems from his utilization of a photomultiplier, which is essentially a point detector, rather than a photodetector array for capturing light signals.

After this basic research, subsequent investigations in this section can be categorized into 2 distinct approaches: the utilization of optical fiber light guides and homemade light guides.

For the former, the origins could be retraced to a US patent awarded in 2008 [30]. As illustrated in Fig. 6B, a pivotal attribute of this patent involves the utilization of a glass optical fiber bundle to convey light information from the curved lenslet array to the flat detector array. Figure 6C further delineates the fabrication process for such a light guide bundle. Initially, a fused imaging fiber conduit is created by subjecting an aligned bundle of straight glass fibers to heat. Subsequently, this fused conduit is heated once more at its center and then drawn to create a double-tapered imaging fiber conduit, which is subsequently divided into 2 segments. The segmented imaging fiber taper is further modified by undergoing a second cut to achieve the desired length. Following this, the larger end is shaped into a dome, and the light guide bundle is finalized after polishing both ends.

However, because of the limited bending resistance of glass optical fibers, the FOV of this BCACE is constrained. Plastic optical fibers, known for their superior flexibility and resistance to bending, prove to be more suitable for achieving a broader FOV. Consequently, in Ma's works [31,32,52–57] on BCACEs, plastic optical fibers were integrated with postprocessing algorithms to accomplish imaging [31] and orientation detection [32], respectively. For instance, a single photodetector is used to replace the photodetector array in capturing light information from all optical fibers, as illustrated in Fig. 6D. Subsequently, a single-pixel imaging technique is utilized to reconstruct the image [31]. In addition, an image sensor is used to record light information from optical fibers, as depicted in Fig. 6E, followed by the utilization of a neural network to detect the target's orientation [32]. Similarly, Krishnasamy et al. [33] used fiber bundles to assemble a compound eye for object tracking.

While it shows promise to use plastic optical fibers as light guides to replicate NCEs, several limitations still exist. First, the overall size is prohibitively large because of the dimensions of the plastic optical fibers used. Second, FOV remains insufficient and can be enhanced through modifications to the 3D structure. Third, direct imaging of the current design proves challenging because of the discrete distribution of plastic optical fibers and the wide acceptance angle of each fiber. Fourth, both imaging and dynamic detection require postprocessing, necessitating either sequential pattern projection on the BCACE (single-pixel imaging [58]) or extensive prior knowledge (neural network [59]). These factors impede practical applications.

Another concept involves the utilization of homemade light guides. Dai et al. [34] suggested using silicone as the light guide core (with a refractive index of 1.50, as depicted in Fig. 6F), along with UV-curable diacrylate polymer serving as the light guide cladding (with a refractive index of 1.46, constituting the substrate in Fig. 6F). By adopting this approach, light can be efficiently transmitted from a curved surface to a planar image sensor. Nevertheless, it is important to note that this method faces limitations in terms of fabrication and still exhibits a constrained FOV.

The integration of a curved microlens array, light guides, and photodetectors closely mimics the anatomical structure of NCEs, effectively circumventing the challenges associated with fabricating photodetector arrays within curved surfaces. Consequently, this approach holds the most promise for further enhancing the performance of BCACEs. However, these BCACEs still exhibit certain limitations. For instance, FOV is constrained, and it is challenging to simultaneously fulfill static imaging and dynamic motion detection within a single BCACE. In addition, the acceptance angle of an individual ommatidium remains relatively large.

One additional point worth mentioning is that a microlens array integration with light guides can serve not only for imaging and dynamic motion detection but also for illumination when the light propagation direction is reversed, i.e., from the light guide to microlenses. For instance, Liu et al. [35] previously suggested the incorporation of a microlens array at the

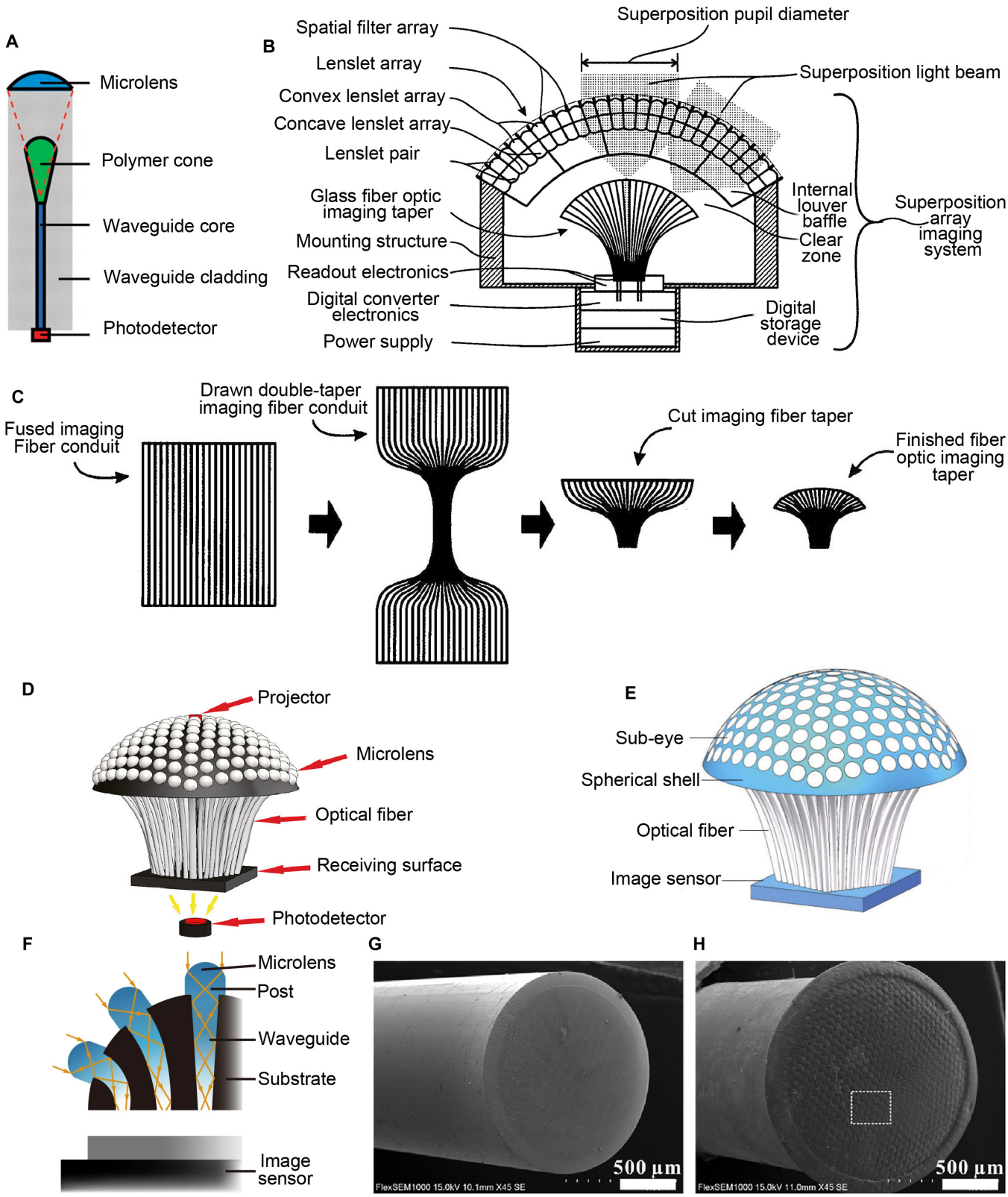


**Fig. 6.** BCACEs with light guides. (A) Artificial ommatidium proposed by Jeong's group. Reprinted with permission from [29] © The American Association for the Advancement of Science. (B) Schematic cross-sectional view of an array imaging system. (C) Schematic flow diagram showing the process steps to fabricate a light guide bundle [30]. (D) Schematic diagram of a single-pixel BCACE. Reprinted with permission from [31] © Elsevier. (E) Schematic diagram of a BCACE mimicking bee's eyes. Reprinted with permission from [32] © Optica Publishing Group. (F) Labeled cross-section of a BCACE with home-made light guides. Reprinted with permission from [34] © Springer Nature. (G and H) Integration of a microlens array and a plastic optical fiber used for illumination. Reprinted with permission from [35] © Optica Publishing Group. (G) Polished original planar plastic optical fiber end face. (H) Fabricated plastic optical fiber end face.

distal end of a plastic optical fiber, as depicted in Fig. 6G and H. When light is introduced from the far opposite end of the plastic optical fiber, the microlens array improves the evenness of light emission over a broad FOV.

## BCACEs with tunable focal lengths

The direct approach for modifying the focal length of compound eyes involves the manipulation of the microlenses distributed along the surface of the macrobase. In certain studies, the alteration of microlenses alone is used to adjust focal lengths, while in other studies, modifications are made not only to the microlenses but also to the macrobase itself, thereby enabling adjustments to the FOV. Specifically, BCACEs of this nature are categorized on the basis of the methods used for tunability.

### *Fluidic pressure*

Among various methods to tune shapes, fluidic pressure is the simplest method. Wei et al. [37] incorporated the structural benefits pertaining to insect apposition NCEs and human eyes to form an adaptive BCACE as shown in Fig. 7A. A big, transparent polymeric membrane, capable of transitioning from a flat surface into a spherical cap with diverse radii of curvature, is utilized to replicate the dome-shaped structure found in insect NCEs. A grid (3 × 3) of lenses, composed of petite transparent polymeric membranes with fluidic structures beneath, is situated atop the big membrane. The focusing power of the lenses can be modified by changing the volume of the fluid, enabling the achievement of an accommodation function. A microfluidic channel network consisting of 2 layers facilitates fluid delivery, allowing for distinct deformation of both the big membrane and the small membranes of individual lenses.

Similarly, Cheng et al. [36] also proposed a BCACE using liquid lenses to minimize defocus aberration. The defocus aberration here refers to the situation where the focal points of microlenses distributed on the curved plane are not aligned on a single common plane, leading to blurred or unclear images. Figure 7B depicts the model, encompassing the object plane, the compound eye, the aperture array, and the image plane. Each individual microlens within the compound eye is saturated with a kind of liquid optical medium, enclosed in a microcavity sealed by a polydimethylsiloxane (PDMS) membrane. Within the same ring, an annular liquid microchannel is incorporated into the sidewall of the cavity to facilitate the injection of liquid, thereby connecting the microlenses. As the liquid is introduced or removed from the liquid microchannel through a syringe pump, the PDMS membrane undergoes deformation, leading to an alteration of the focal length. In various rings, the liquid lenses exhibit distinct optical characteristics, whereas those

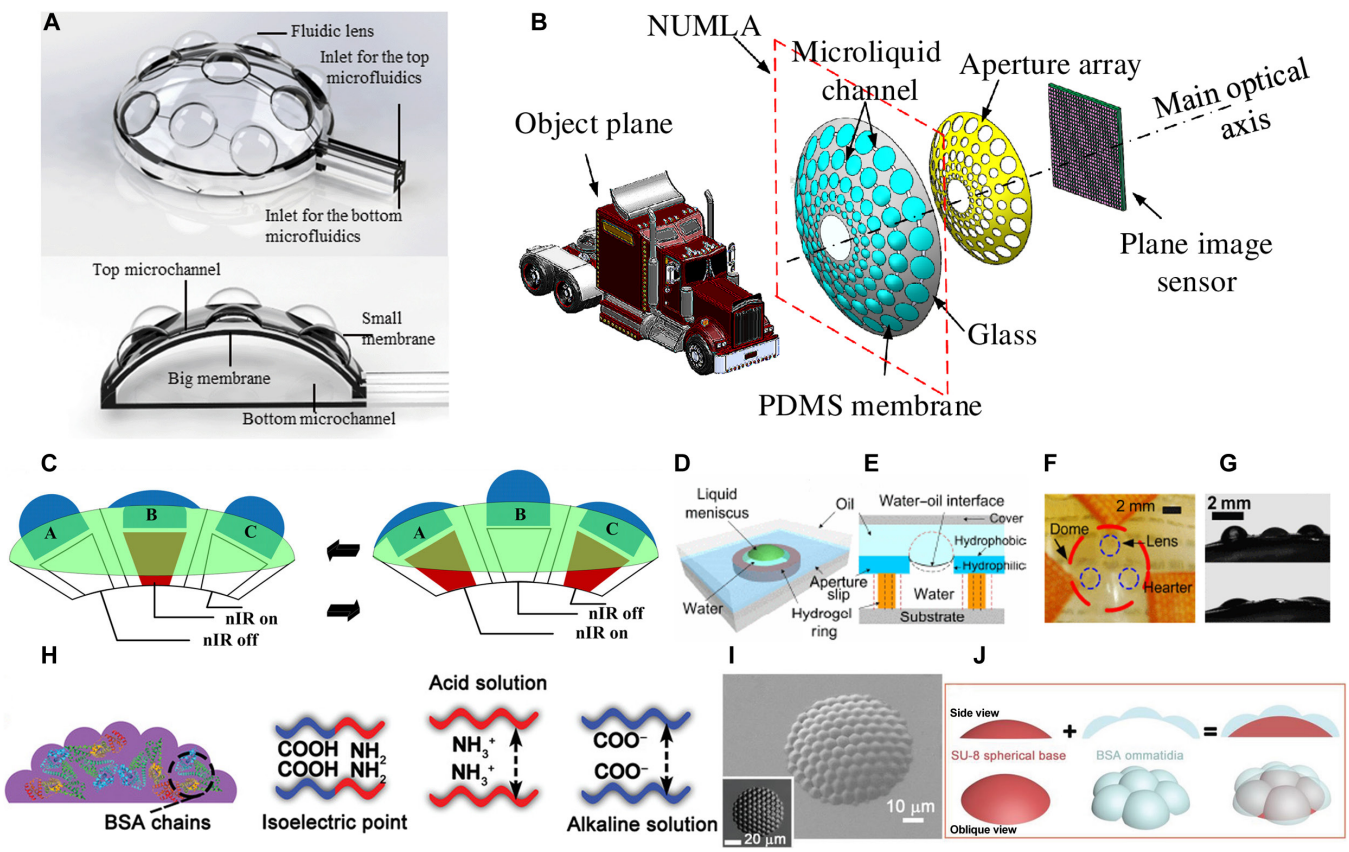


**Fig. 7.** BCACEs with tunable focal lengths. (A) Working principle of the BCACE which distributes an array of membrane-encased fluidic lenses on a big flexible membrane. Reprinted with permission from [37] © Royal Society of Chemistry. (B) Schematic diagram of the BCACE with self-adaptive focal length adjustment to minimize defocus aberration. NUMLA, nonuniform microlens array model. Reprinted with permission from [36] © Optica Publishing Group. (C) Adaptation of the microscopic lens shapes under nIR irradiation. Reprinted with permission from [38] © American Chemical Society. (D and E) Structure and mechanism of an adaptable focus microlens controlled by a thermoresponsive hydrogel ring. (D) 3D diagram of a single microlens. (E) Cross-section of a single microlens. Reprinted with permission from [39] © IEEE. (F) Photo of a microlens array with 3 microlenses on a glass hemisphere. (G) Lateral view of the water droplets at 2 different temperatures (top: 23 °C; bottom: 55 °C). Reprinted with permission from [39] © IEEE. (H) Fundamental mechanism of protein-based BCACEs with adjustable features. Reprinted with permission from [40] © John Wiley and Sons. (I and J) Protein-based BCACEs. (I) SEM image of the entire protein-based BCACE, and the inset is an optical microscopy image. (J) Illustrative representation of the composite BCACE comprising a passive SU-8 hemispherical macrobase and active BSA-based microlenses. Reprinted with permission from [40] © John Wiley and Sons.

within the same ring share identical parameters. Likewise, the aperture array serves to prevent optical signal interference.

#### *Thermal effect*

The thermal effect provides another way to change the focal lengths of BCACEs. Wang et al. [38] proposed a kind of graphene-based BCACE as shown in Fig. 7C. All microlenses are fabricated with graphene nanosheets (GNSs) that can absorb energy and convert it to thermal energy when driven by near-infrared (nIR) pulsed laser irradiation based on Maxwell's electromagnetic wave theory [60,61], resulting in the increment of the temperature of microlenses. Correspondingly, the pressure differential at the air-solution interface, which directly dictates the configuration of the liquid meniscus, will be tuned with the increment of the temperature based on Adamson's theoretical model [62,63]. Hence, when nIR irradiation is activated, the photothermal conversion initiated by GNSs prompts the liquid in the microlenses to escape from the microcavity. Conversely, when the nIR laser is deactivated, the resulting cooling leads to the liquid within the microlenses retracting back into the microcavity, i.e., shapes of microlenses are tuned with changes of the nIR laser conditions. In this way, every microlens on the surface of the macrobase is tuned precisely.

Similarly, Zhu et al. [39] utilized a thermoresponsive and reversible hydrogel ring made of *N*-isopropyl acrylamide as a microactuator for fine-tuning the focal length. With a decrease in temperature from above to below the lower critical solution temperature of the hydrogel, the hydrogel absorbs water and undergoes swelling. As the volume alteration induced by water in the cavity is less pronounced than in the hydrogel ring, it results in a net volume change that governs the curvature of the water–oil meniscus as shown in Fig. 7D and E. Therefore, the focal lengths of these liquid microlenses can be adjusted by altering the environmental temperature. To validate this principle, in that paper, an array consisting of 3 microlenses, denoted by smaller dashed line circles in Fig. 7F, is positioned onto a hemispherical glass dome. A small resistor is positioned adjacent to each microlens to regulate the local temperature. Figure 7G illustrates the lateral view of the water menisci at various temperatures. The upper image was captured at 23 °C, whereas the lower one was taken at 55 °C, revealing a significant alteration in the curvature radius of the water–air meniscus.

#### *pH*

Inspired by the adaptable crystalline lens, which is aided by the ciliary muscles of the human eye, BCACEs here are fabricated with bovine serum albumin (BSA) protein [40]. Figure 7H illustrates the pH-induced actuation mechanism, which is ascribed to the existence of carboxyl groups and amino groups linked at the isoelectric point within the BSA molecular chains. These groups can undergo deprotonation or protonation based on varying pH levels [64–67]. The electrostatic interaction among these groups induces the expansion or contraction of BSA structures, resulting in alterations in the focal length. Similarly, to verify the principle, based on whether the FOV can be altered, 2 types of BCACEs are proposed: entire protein-based BCACE and composite BCACE. The former is fabricated with BSA entirely, so with variations in the pH of the surrounding environment, the macrobase and microlenses are concurrently adjusted, resulting in an adaptable FOV and focal length (Fig. 7I). The latter comprises a macrobase made with chemically inert SU-8 and microlenses made with BSA, resulting in the focal length being solely tuned at a fixed FOV (Fig. 7J).

In this section, we have analyzed 3 methods used to modify the focal lengths of BCACEs. It is worth noting that in addition to these 3 mentioned methods used in BCACEs, there are numerous other techniques available for adjusting the focal lengths of microlenses, which have not yet been utilized in BCACEs. The integration of these methods with BCACEs holds the potential for substantial advancements, which will be further elaborated upon in the subsequent discussion section.

## Fabrication Methods

### Fabrication of curved microlens arrays used in BCACEs

The common approach for producing a curved microlens array involves a combination of lithography, thermal embossing, and gas-assisted deformation. For example, Lian et al. [23] combined these methods to form a BCACE as shown in Fig. 8A to J. First, the photoresist is spin-coated on a silicon substrate, and a conventional lithography procedure is used to transfer the mask patterns onto the photoresist (Fig. 8A). After that, the plasma etching process is used to transfer the patterns onto the silicon wafer (Fig. 8B and C). Next, a passivation layer is developed on the mold's surface to ease the demolding process (Fig. 8D). Furthermore, a polymer (cycloolefin copolymer, 500 μm in thickness) is pressed under a pressure of 200 mbar at 145 °C for 6 min (thermal embossing; Fig. 8E). After purging with nitrogen gas for 10 min and cooling to 80 °C, it is possible to detach the polymeric microlenses with different focal lengths (Fig. 8F). What's more, soft lithography (Fig. 8G) and gas-assisted deformation (Fig. 8H) are used for pattern transfer and the conversion from a planar to a curved structure. Subsequently, a photosensitive resin is poured onto the deformed membrane and solidified by exposure to UV light (Fig. 8I). Finally, the BCACE with multifocal microlenses is obtained successfully (Fig. 8J). Besides, the curved microlens array can also be manufactured using a combination of lithography and a 2-step thermal reflow process [68].

Li et al. [69] also proposed the integration of inkjet printing and air-assisted deformation to form a BCACE. Figure 8K to M demonstrates the inkjet printing procedure for the microlens array. First, the microlens morphology is governed by precisely controlling the quantity of droplets deposited in the identical location with a high degree of accuracy. Subsequently, the device is annealed for 15 min at 90 °C, exposed to UV treatment until full cross-linking is achieved, and then subjected to an additional 30-min annealing at 100 °C. As a result, a planar microlens array is obtained. Figure 8N to P demonstrates the air-assisted deformation process. In the first step, PDMS is used for the pattern transfer process. Subsequently, the negative air pressure is used to create a deformed elastomer membrane. After achieving pressure stability, solvent-free UV-curable epoxy resin is introduced into the created cavity, covered with a coverslip, and then exposed to UV light for a complete cross-linking process lasting 5 min. Finally, after peeling, the compound eye is produced.

Similarly, Wang et al. [38] proposed the creation of a BCACE based on GNSs using air-assisted deformation, as illustrated in Fig. 8R to W. Following the formation of a transparent hemispheric dome through the mentioned air-assisted deformation, numerous microcavities are retained within this dome (Fig. 8R to T). Subsequently, the dome is immersed in a vacuum beaker filled with glycerol/GNSs solution before being withdrawn (Fig. 8U and V). Ultimately, the droplet is adsorbed into

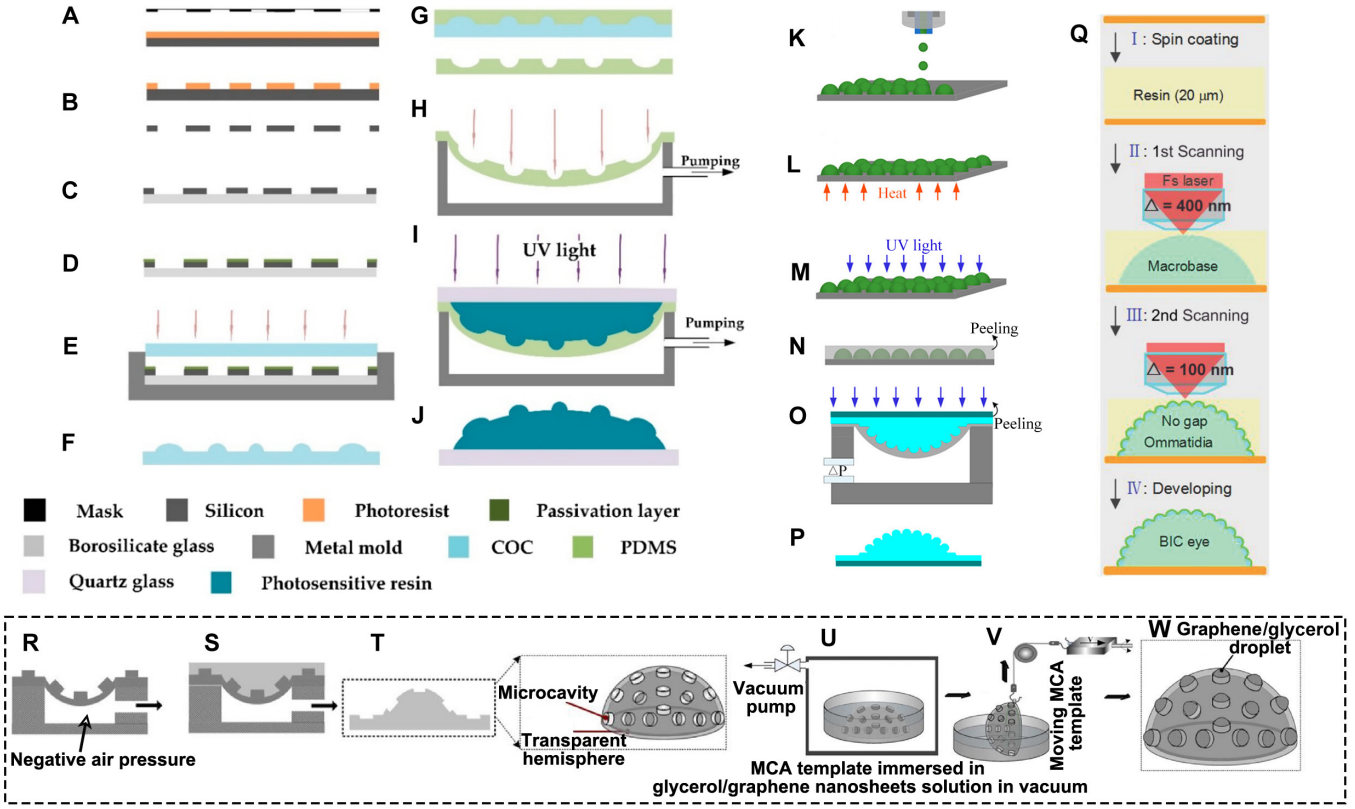


**Fig. 8.** Examples of BCACE fabrication processes. (A to J) Schematic diagram of the fabrication process combining lithography, thermal embossing, and gas-assisted deformation. COC, cycloolefin copolymer. Reprinted with permission from [23] © MDPI. (A) Photoresist spin-coated on a silicon substrate and exposed. (B) Development and etching of silicon wafers. (C) Bonding of patterned silicon substrate to borosilicate glass. (D) Growth of a passivation layer on the surface. (E) Heating and pressing of the polymer. (F) Polymer peeled off to get a microlens array pattern. (G) Replication of the structure on the polymer using PDMS. (H) Deformation of the PDMS membrane and packaging in a sealed cavity under a pressure difference. (I) Pouring and curing of a photosensitive adhesive. (J) BCACE peeled off. (K to P) Schematic diagram of the fabrication process combining inkjet printing and air-assisted deformation. Reprinted with permission from [69] © American Chemical Society. (K to M) Fabrication of the microlens array. (K) A microlens array fabricated through inkjet printing, where the geometry and dimensions of the microlens are regulated by the number of superimposed drops. (L and M) Heating and UV irradiation. (N) PDMS molding. (O) Membrane deformation. (P) Formation of the BCACE. (Q) Schematic for the fabrication of a BCACE by the laser direct writing method. Reprinted with permission from [21] © John Wiley and Sons. (R to W) Fabrication of BCACE based on GNSs. Reprinted with permission from [38] © American Chemical Society. (R) PDMS elastomer membrane shaped into a hemispheric dome under negative air pressure. (S) UV-curable epoxy resin dispensed on deformed elastomer, fully cross-linked. (T) Microcavity array (MCA) template resulted from manually peeling off the NOA (Norland Optical Adhesives) hemispheric shell. (U) MCA template vacuum-immersed in glycerol/GNSs solution to fill each microcavity. (V) Beaker with glycerol/GNSs solution, where the MCA template moves at 0.16 mm·s$^{-1}$ and the temperature is maintained at 15 °C. (W) BCACE with GNSs serving as microlenses.

the microcavity, facilitated by the capillary breakup, serving the purpose of a GNS-based microlens (Fig. 8W).

Recently, the femtosecond laser direct writing technology has become a promising method because of its effective ability to realize various 3D complex microstructures and high precision [21,22,40,70–72]. For example, the femtosecond laser direct writing technology is used to obtain microlenses with sizes as small as micrometers [21], as shown in Fig. 8Q. After spin-coating the resin, the macrobase and microlenses are fabricated, respectively, by forming voxels with different dimensions, thus producing the curved microlens array used in BCACEs.

The aforementioned fabrication methods can be broadly classified into 2 types. The first involves the initial formation of a 2D lens array, followed by deformation into a 3D lens array through fluid-assisted techniques. The second type uses laser direct writing technology to directly generate a 3D lens array. The first type, upon the creation of a 3D lens array template, facilitates batch production; however, because of constraints in the processing methods of 2D lens arrays, lenses in this category tend to exhibit a relatively undiversified nature. Correspondingly, the second type of solution possesses a higher degree of processing freedom, allowing for the fabrication of lenses with diverse shapes, while sacrificing some fabrication time and cost.

## Integration of BCACEs

This integration can be categorized into 2 distinct types: (a) the integration of a curved microlens array and a photodetector array a within curved surface and (b) the integration of a curved microlens array, optical light guides, and a planar photodetector array.

Regarding the first type, an initial step involves the integration of a planar microlens array with a planar photodetector array, ensuring precise alignment between each microlens and its corresponding photodetector. Subsequently, this combined structure is flexed or curved to conform to a predetermined curved surface design.

As for the second type, when optical fibers serve as light guides, a preperforated 3D structure is typically fabricated at the outset. Following this, optical fibers are threaded through preformed apertures. In cases where homemade light guides are used, an initial step involves the fabrication of a host structure

(for instance, through methods such as projection micro stereolithography 3D printing). Subsequently, a liquid light guide is introduced into preestablished channels, utilizing techniques such as microfluidic-assisted molding. The liquid light guide is then solidified through a curing process, resulting in the formation of an elastomeric connection. These processes effectively establish the connection of the light guides to other system components.

## Applications

Although the planar microlens array has been applied widely, for example, in the endoscopic system [73–75], intraoral diagnosis [76–78], and photolithography [79], when it comes to the application of BCACEs, it primarily focuses on the detection of motion. Noteworthily, the detection of motion focuses on recognizing motion behaviors through consecutive frames of a scene that encompasses various techniques such as capturing optical flow fields, while the conventional capture of video-rate images emphasizes the process of recording a rapid succession of frames to produce a video. Importantly, BCACEs possess unique merits in the detection of motion. For example, its wide FOV helps BCACEs to excel in motion detection under a wide field compared with common cameras, and, thus, BCACEs are more fitting for being applied in areas such as obstacle avoidance. In the future, if BCACEs mimicking superposition NCEs make huge progress, they will also be more effective in detecting motion under dim-light conditions compared with common cameras.

Specifically, Leitel et al. [80] qualitatively measured the optics flow fields for yaw and pitch rotation with the BCACE mentioned before [25], as shown in Fig. 9A, where the optical flow vectors' direction represented motion direction and length represented motion velocity. Similarly, Yoo et al. [81] proposed to combine the BCACE and the convolutional neural network to achieve the ego-motion (the movement of the camera itself, rather than the transition between 2 scenes) classification.

Ulteriorly, to test the linear motion and circular motion quantitatively, Pang et al. [82] proposed a 7-microlens BCACE, as shown in Fig. 9B. The experimental setup is arranged as depicted in Fig. 9C. Throughout the experiment, the light-emitting diode target underwent a circular motion within the *x*-*y* plane, while the translation stage executed linear motion at a rate of 10 mm·s$^{-1}$ in the *z* direction, spanning a range from 100 to 200 mm. Figure 9D illustrates an exquisite match between the reconstructed *z* value and the true *z* value, where the diagonal line of Fig. 9D represents the true *z* value since the translation stage moves at a constant speed between 100 and 200mm. Correspondingly, Fig. 9E shows that the reconstructed *x* and *y* coordinates follow a circle relationship whose diameter closely matches the true diameter of the circular motion. Therefore, the possibility of using BCACEs in motion detection is quantitatively researched.

Although, in some essays, so-called BCACEs were proposed [83–85], these systems, which disperse several cameras on curved structures, possessing large volumes and high weights, in reality, are not compact BCACEs. For instance, Floreano et al. [83,84] proposed a vision system that was used by unmanned aerial vehicles to evade obstacles, as shown in Fig. 9F. Similarly, for the purpose of extracting self-motion parameters of ground-moving robots from optical flow to surprisingly high precision,

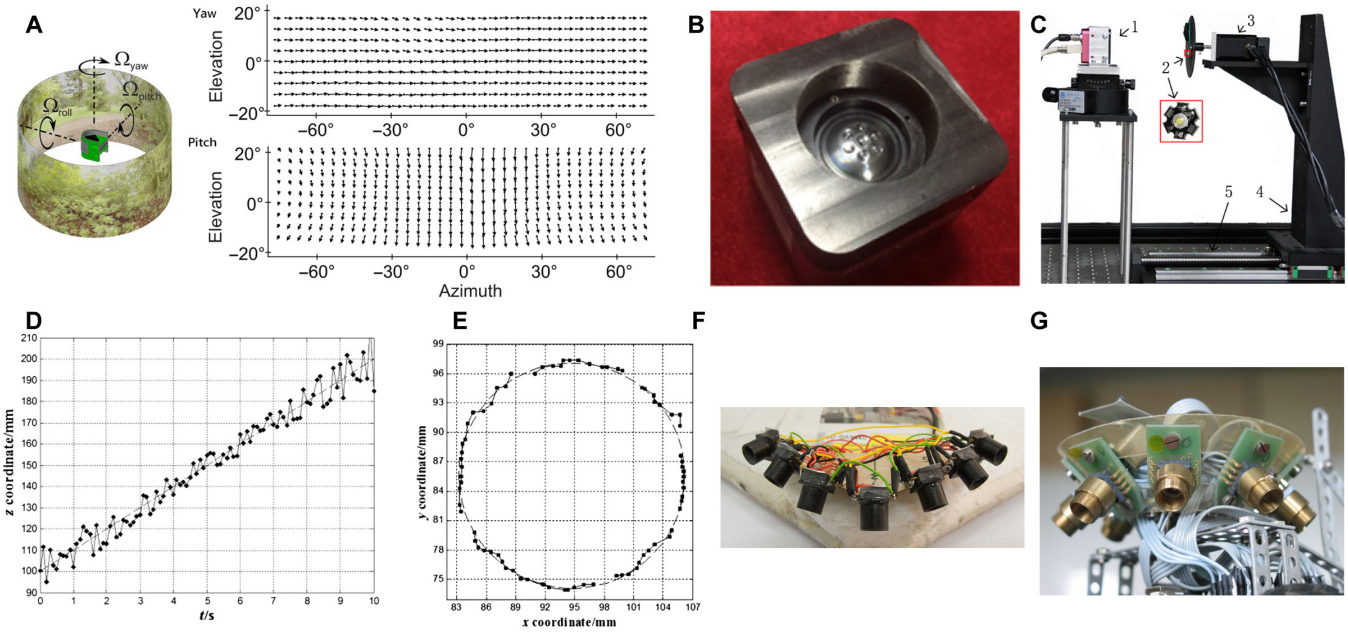


**Fig. 9.** Applications of BCACEs. (A) BCACE placed inside a circular arena lined with a natural pattern. It captures optical flow fields, which are depicted in a Mercator projection, showcasing yaw and pitch rotations at 22°·s$^{-1}$. Reprinted with permission from [25] © Proceedings of the National Academy of Sciences. (B to E) BCACE used to test linear and circular motion. Reprinted with permission from [82] © Optica Publishing Group. (B) Seven-microlens BCACE. (C) Experimental setup. (1) Bionic compound eye system. (2) Light-emitting diode target. (3) Speed motor. (4) Translation stage. (5) Horizontal guide rail. (D) Reconstructed *z* values from 100 to 200 mm. (E) Reconstructed *x*-*y* locations at 150 mm. (F) Close-up view of a BCACE consisting of 7 optic flow sensors used by unmanned aerial vehicles. The viewing directions are oriented toward each side and below the aircraft, with an eccentricity angle of 45° and azimuthal angles of 90°, 120°, 150°, 180°, 210°, 240°, and 270°, respectively. Reprinted with permission from [84] © Springer Nature. (G) BCACE containing 8 optical mouse sensors, each looking at a 45° angle relative to each other in azimuth and inclined approximately −45° in relation to the horizon, toward the ground. Reprinted with permission from [85] © MDPI.

a prototype of a sensor head featuring 8 sensors, each oriented at angular intervals of 45° from one another in azimuth, and looking downward to the ground at an angle of −45° below the horizon is illustrated in Fig. 9G [85].

While BCACEs have made substantial progress in motion detection, they still have a considerable journey ahead to meet requirements beyond laboratories. These challenges encompass small-scale, high-rate, and complex motions, among other factors, all of which are indispensable for practical applications. Moreover, other applications (such as real-time panoramic imaging with high resolution) demand higher performance from BCACEs. Consequently, there is still a considerable path to be traversed before BCACEs can find broader applications.

## Discussion

### Further emulation of NCEs

While BCACEs have made substantial advancements in recent decades, they still have a considerable distance to cover when compared to their natural counterparts. For instance, in comparison to a worker bee, which possesses thousands of ommatidia (approximately 4,883 ± 10 for *Megalopta genalis* [86]), with each ommatidium featuring an acceptance angle of just several degrees (about 2.5° for *Apis mellifera* [87]), despite the potential promise offered by certain techniques, such as the use of femtosecond lasers, in fabricating a substantial quantity of microlenses, it remains exceedingly challenging to generate an equivalent number of complete ommatidia (i.e., not solely microlenses). Hence, novel designs and fabrication approaches become imperative to bridge this existing gap. For instance, Yang et al. [88,89] proposed the fabrication of BCACEs by replicating the anatomical structure of NCEs with PDMS in recent years, offering a potential solution to bridge this gap in the future. Besides, the flexibility of the optic superposition compound eyes due to the pigment migration in the clear zone and the balance between resolution and optical sensitivity of the neuron superposition compound eyes due to the anatomic complex attribute researchers to further mimic NCEs.

### Further combination of BCACEs and optofluidic tunable lenses

One of the pivotal constituents within compound eyes resides in their microlenses. Notably, optofluidic tunable lenses have emerged as a burgeoning research domain in recent years. The application of these methods possesses the capability to greatly boost the performance of BCACEs in focal length modulation and image aberration correction, such as spherical aberration. For instance, considering focal length adjustment, there are 2 principal approaches available: altering the microlens geometry and modifying the refractive index.

With regard to the former aspect, there are numerous methodologies available for implementation. For instance, the electrowetting effect is capable of altering the wetting characteristics, such as the contact angle, of a liquid on a solid substrate by applying an electric field to modify the shape of liquid microlenses [90]. The dielectrophoresis effect governs the motion of neutral particles, induced by the polarization effect within a nonuniform electric field, resulting in the modification of the microlens configuration [91,92]. Electrostatic forces influence the distribution of the liquid, which is determined by the separation distance between 2 parallel electrode plates. Specifically, it allows for the adjustment of the liquid distribution by manipulating the applied voltage to both plates, thereby enabling changes in the microlens shape in accordance with alterations in the liquid distribution [93]. Furthermore, an array of methods, including piezoelectric elements [94], thermoelectric elements [95], liquid crystal elastomers [96], pneumatic pumps [97], hydraulic pumps [98], ultrasonic transducers [99], micromechanical motors [100], and others, can all be used to modify the shape of liquid microlenses. These methods can subsequently be harnessed to manipulate the focal length and even correct aberrations.

In the context of the latter consideration, it is noteworthy that the refractive index is contingent upon a multitude of factors, notably including concentration [101,102] and temperature [103]. Within the confines of a laminar flow regime occurring within microchannels, the concentration gradient is primarily governed by the process of solution diffusion [104], which can be dynamically adjusted via meticulous control of flow rates. Yang et al. [105] posited that the refractive gradient could be judiciously manipulated through the diffusion phenomenon between ethylene glycol and deionized water. In a similar vein, Mao et al. [101] substantiated the prospect of reconfiguring the refractive gradient through the use of a $CaCl_2$ solution (core) and deionized water (cladding). Temperature conduction stands out as another potent means of engineering a refractive profile. Tang et al. [106] advanced the concept of a thermally induced optical waveguide, using streams at varying temperatures to orchestrate the optical behavior. This method involves the use of 2 streams, one at a higher temperature (forming the cladding), to encase another stream at a lower temperature (representing the core), thus creating a noticeable temperature gradient along the channel. Importantly, the optical characteristics of the liquid waveguide can be facilely tailored by modulating the flow rate. Furthermore, Chen et al. [107,108] introduced an optofluidic tunable lens predicated on the creation of a refractive index gradient via laser-induced thermal gradients at the microscale, thereby facilitating precise focusing.

The primary challenge associated with implementing these techniques within ACEs pertains to the distribution of optofluidic tunable lenses across a curved surface and their compact integration with other components, including light guides. Nonetheless, this presents a promising avenue for enhancing the overall performance of BCACEs.

## Conclusions

This paper has provided a comprehensive review of BCACEs. Rooted in the foundational underpinnings of NCEs and BCACEs, we have introduced a set of parameters to delineate the characteristics of BCACEs. The reviewed BCACEs are categorized into 2 primary types based on their working principles: those with fixed focal lengths and those with tunable focal lengths. In particular, the former type can be further subdivided into 3 categories, namely, simplified BCACEs, BCACEs with photodetector arrays within curved surfaces, and BCACEs with light guides. The latter type can also be categorized on the basis of various techniques for altering the shapes of microlenses, including fluidic pressure, thermal effects, and pH adjustments.

Concerning fabrication, while some innovative methods such as laser direct writing have been proposed for creating curved microlens arrays used in BCACEs, the production of

a complete BCACE system that can rival the performance of sophisticated NCEs remains an exceedingly challenging task. Consequently, BCACEs still have a considerable journey ahead. For instance, novel design concepts and fabrication approaches need to be developed to emulate not only apposition NCEs but also optic superposition NCEs and neural superposition NCEs. Furthermore, the integration of BCACEs with optofluidic tunable lenses enables precise control over light manipulation, thereby facilitating the realization of artificial intelligence systems with enhanced information processing capabilities.

In summary, it is foreseeable that BCACEs will transform micro-optical imaging systems into versatile platforms for practical applications, including but not limited to smart healthcare [109], intelligent robotic vision systems [110], and unmanned aerial vehicle vision systems [111].

## Acknowledgments

**Funding:** This work was supported by the Research Grants Council of Hong Kong (15215620 and N_PolyU511/20), Innovation and Technology Commission of Hong Kong (ITF-MHKJFS MHP/085/22), and The Hong Kong Polytechnic University (1-CD4V, 1-YY5V, 1-CD6U, G-SB6C, 1-CD8U, 1-BBEN, 1-W28S, and 1-CD9Q). The technical communication about fabrication methods with the UMF-Materials Research Centre and UMF-Cleanroom of the University Research Facility in Material Characterization and Device Fabrication (UMF), and the Surface Engineering Unit of the Additive Manufacturing Stream, Industrial Centre of The Hong Kong Polytechnic University is acknowledged as well.
**Author contributions:** H.J. conducted the survey and wrote the manuscript. C.C.T. and L.S. contributed to data collection. W.Y., H.F., M.M., and Y.J. assisted conceptualization and classification. X.Z. set the scope of contents, discussed the technical details, and revised the manuscript.
**Competing interests:** The authors declare that they have no competing interests.

## References

1. Hooke R, Martyn J, Allestry J. *Micrographia, or some physiological descriptions of minute bodies, made by magnifying glasses, with observations and inquiries thereupon*. London (UK): Printers to Council of the Royal Society of London; 1664.
2. Exner S. *Die Physiologie der facettirten Augen von Krebsen und Insecten: eine Studie*. Leipzig (Germany): Franz Deuticke; 1891.
3. Land MF. Compound eyes: Old and new optical mechanisms. *Nature*. 1980;287(5784):681–686.
4. Lee LP, Szema R. Inspirations from biological optics for advanced photonic systems. *Science*. 2005;310(5751):1148–1150.
5. Chen J, Zhou Z, Kim BJ, Zhou Y, Wang Z, Wan T, Yan J, Kang J, Ahn JH, Chai Y. Optoelectronic graded neurons for bioinspired in-sensor motion perception. *Nat Nanotechnol*. 2023;18(8):882–888.
6. De Ruyter van Steveninck RR, Laughlin SB. The rate of information transfer at graded-potential synapses. *Nature*. 1996;379(6566):642–645.
7. Liang WL, Pan JG, Su GDJ. One-lens camera using a biologically based artificial compound eye with multiple focal lengths. *Optica*. 2019;6(3):326–334.
8. Kagawa K, Yamada K, Tanaka E, Tanida J. A three-dimensional multifunctional compound-eye endoscopic system with extended depth of field. *Electron Commun Jpn*. 2012;95(11):14–27.
9. Lecoeur J, Baird E, Floreano D. Spatial encoding of translational optic flow in planar scenes by elementary motion detector arrays. *Sci Rep*. 2018;8(1):5821.
10. Ong JM, da Cruz L. The bionic eye: A review. *Clin Exp Ophthalmol*. 2012;40(1):6–17.
11. Nussbaum P, Voelkel R, Herzig HP, Eisner M, Haselbeck S. Design, fabrication and testing of microlens arrays for sensors and microsystems. *Pure Appl Opt*. 1997;6(6):617.
12. Brückner A, Duparré J, Leitel R, Dannberg P, Bräuer A, Tünnermann A. Thin wafer-level camera lenses inspired by insect compound eyes. *Opt Express*. 2010;18(24):24379–24394.
13. Tanida J, Kumagai T, Yamada K, Miyatake S, Ishida K, Morimoto T, Kondou N, Miyazaki D, Ichioka Y. Thin observation module by bound optics (TOMBO): An optoelectronic image capturing system. *Proc SPIE*. 2000;4089:1030–1036.
14. Shankar M, Willett R, Pitsianis NP, Te Kolste R, Chen C, Gibbons R, Brady DJ. Ultra-thin multiple-channel LWIR imaging systems. Paper presented at: Infrared and Photoelectronic Imagers and Detector Devices II. SPIE; 2006 Sep 7; San Diego, CA, USA.
15. Ren H, Wu ST. Tunable-focus liquid microlens array using dielectrophoretic effect. *Opt Express*. 2008;16(4):2646–2652.
16. Fan CY, Lin CP, Su GDJ. Ultrawide-angle and high-efficiency metalens in hexagonal arrangement. *Sci Rep*. 2020;10(1):15677.
17. Fan ZB, Qiu HY, Zhang HL, Pang XN, Zhou LD, Liu L, Ren H, Wang QH, Dong JW. A broadband achromatic metalens array for integral imaging in the visible. *Light: Sci & Applic*. 2019;8(1):67.
18. Salmanogli A, Geçm HS, Piskin E. Plasmonic system as a compound eye: Image point-spread function enhancing by entanglement. *IEEE Sensors J*. 2018;18(14):5723–5731.
19. Kogos LC, Li Y, Liu J, Li Y, Tian L, Paiella R. Plasmonic ommatidia for lensless compound-eye vision. *Nat Commun*. 2020;11(1):1637.
20. Li L, Hao Y, Xu J, Liu F, Lu J. The design and positioning method of a flexible zoom artificial compound eye. *Micromachines*. 2018;9(7):319.
21. Wu D, Wang JN, Niu LG, Zhang XL, Wu SZ, Chen QD, Lee LP, Sun HB. Bioinspired fabrication of high-quality 3D artificial compound eyes by voxel-modulation femtosecond laser writing for distortion-free wide-field-of-view imaging. *Adv Optic Mater*. 2014;2(8):751–758.
22. Jin GX, Hu XY, Ma ZC, Li CH, Zhang YL, Sun HB. Femtosecond laser fabrication of 3D templates for mass production of artificial compound eyes. *Nanotechnol Precis Eng (NPE)*. 2019;2(3):110–117.
23. Lian G, Liu Y, Tao KK, Xing H, Huang R, Chi M, Zhou W, Wu Y. Fabrication and characterization of curved compound eyes based on multifocal microlenses. *Micromachines*. 2020;11(9):854.
24. Song YM, Xie Y, Malyarchuk V, Xiao J, Jung I, Choi KJ, Liu Z, Park H, Lu C, Kim RH, et al. Digital cameras with designs inspired by the arthropod eye. *Nature*. 2013;497(7447):95–99.
25. Floreano D, Pericet-Camara R, Viollet S, Ruffier F, Brückner A, Leitel R, Buss W, Menouni M, Expert F,

Juston R, et al. Miniature curved artificial compound eyes. *Proc Natl Acad Sci USA*. 2013;110(23):9267–9272.
26. Lee WB, Jang H, Park S, Song YM, Lee HN. COMPU-EYE: A high resolution computational compound eye. *Opt Express*. 2016;24(3):2013–2026.
27. Lee M, Lee GJ, Jang HJ, Joh E, Cho H, Kim MS, Kim HM, Kang KM, Lee JH, Kim M, et al. An amphibious artificial vision system with a panoramic visual field. *Nat Electron*. 2022;5(7):452–459.
28. Pericet-Camara R, Dobrzynski MK, Juston R, Viollet S, Leitel R, Mallot HA, Floreano D. An artificial elementary eye with optic flow detection and compositional properties. *J R Soc Interface*. 2015;12(109):20150414.
29. Jeong KH, Kim J, Lee LP. Biologically inspired artificial compound eyes. *Science*. 2006;312(5773):557–561.
30. Reininger FM. Fiber coupled artificial compound eye. U.S. Patent 7376314B2; 2008 May 20.
31. Ma MC, Zhang Y, Deng H, Gao X, Gu L, Sun Q, Su Y, Zhong X. Super-resolution and super-robust single-pixel superposition compound eye. *Opt Lasers Eng*. 2021;146:Article 106699.
32. Ma MC, Li H, Gao XC, Si WH, Deng HX, Zhang J, Zhong X, Wang K. Target orientation detection based on a neural network with a bionic bee-like compound eye. *Opt Express*. 2020;28(8):10794–10805.
33. Krishnasamy R, Thomas P, Pepic S, Wong W, Hornsey RI. Calibration techniques for object tracking using a compound eye image sensor. *Networks*. 2004;5611:42–52.
34. Dai B, Zhang L, Zhao C, Bachman H, Becker R, Mai J, Jiao Z, Li W, Zheng L, Wan X, et al. Biomimetic apposition compound eye fabricated using microfluidic-assisted 3D printing. *Nat Commun*. 2021;12(1):6458.
35. Liu F, Yang Q, Bian H, Zhang F, Hou X, Kong D, Chen F. Artificial compound eye-tipped optical fiber for wide field illumination. *Opt Lett*. 2019;44(24):5961–5964.
36. Cheng Y, Cao J, Meng L, Wang Z, Zhang K, Ning Y, Hao Q. Reducing defocus aberration of a compound and human hybrid eye using liquid lens. *Appl Opt*. 2018;57(7):1679–1688.
37. Wei K, Zeng H, Zhao Y. Insect–human hybrid eye (IHHE): An adaptive optofluidic lens combining the structural characteristics of insect and human eyes. *Lab Chip*. 2014;14(18):3594–3602.
38. Wang L, Li F, Liu H, Jiang W, Niu D, Li R, Yin L, Shi Y, Chen B. Graphene-based bioinspired compound eyes for programmable focusing and remote actuation. *ACS Appl Mater Interfaces*. 2015;7(38):21416–21422.
39. Zhu D, Li C, Zeng X, Jiang H. Hydrogel-actuated tunable-focus microlens arrays mimicking compound eyes. Paper presented at: TRANSDUCERS 2009–2009 International Solid-State Sensors, Actuators and Microsystems Conference; 2009 Jun 21–25; Denver, CO, USA.
40. Ma ZC, Hu XY, Zhang YL, Liu XQ, Hou ZS, Niu LG, Zhu L, Han B, Chen QD, Sun HB. Smart compound eyes enable tunable imaging. *Adv Funct Mater*. 2019;29(38):1903340.
41. Agi E, Langen M, Altschuler SJ, Wu LF, Zimmermann T, Hiesinger PR. The evolution and development of neural superposition. *J Neurogenet*. 2014;28(3-4):216–232.
42. Land MF. *Variations in the structure and design of compound eyes. In: Facets of vision*. Berlin (Heidelberg): Springer; 1989. p. 90–111.
43. Land MF. The optical structures of animal eyes. *Curr Biol*. 2005;15(9):R319–R323.
44. Kirschfeld K. The absolute sensitivity of lens and compound eyes. *Z Naturforsch, C: Biosci*. 1974;29(9-10):592–596.
45. Fischer A, Horstmann G. Fine structure of the eye of the meal moth, Ephestia kuehniella Zeller (Lepidoptera, Pyralididae). *Z Zellforsch Mikrosk Anat*. 1971;116:275–304.
46. Shaw SR. Optics of arthropod compound eye. *Science*. 1969;165(3888):88–90.
47. Berry S. The use of optical coherence tomography to demonstrate dark and light adaptation in a live moth. *Environ Entomol*. 2022;51(4):643–648.
48. Warrant EJ. Seeing better at night: Life style, eye design and the optimum strategy of spatial and temporal summation. *Vis Res*. 1999;39(9):1611–1630.
49. Frederiksen R, Warrant EJ. The optical sensitivity of compound eyes: Theory and experiment compared. *Biol Lett*. 2008;4(6):745–747.
50. Li L, Allen YY. Microfabrication on a curved surface using 3D microlens array projection. *J Micromech Microeng*. 2009;19(10):Article 105010.
51. Li L, Allen YY. Development of a 3D artificial compound eye. *Opt Express*. 2010;18(17):18125–18137.
52. Ma MC, Guo F, Cao ZL, Wang KY. Development of an artificial compound eye system for three-dimensional object detection. *Appl Opt*. 2014;53(6):1166–1172.
53. Deng H, Gao X, Ma M, Li Y, Li H, Zhang J, Zhong X. Catadioptric planar compound eye with large field of view. *Opt Express*. 2018;26(10):12455–12468.
54. Ma MC, Wang KY. Improvement on object detection accuracy by using two compound eye systems. Paper presented at: 7th International Symposium on Advanced Optical Manufacturing and Testing Technologies: Optical Test and Measurement Technology and Equipment; 2014 Sep 18; Harbin, China.
55. He JZ, Jian HJ, Zhu QT, Ma MC, Wang KY. Matching between the light spots and lenslets of an artificial compound eye system. Paper presented at: Applied Optics and Photonics China (AOPC2017); 2017 Oct 24; Beijing, China.
56. Ma MC, Gao XC, Zhang J, Deng HX. Design of a compound eye system with planar micolens array and curved folded mirrors. Paper presented at: 8th International Symposium on Advanced Optical Manufacturing and Testing Technologies: Optical Test, Measurement Technology, and Equipment; 2016 Sep 27; Suzhou, China.
57. Ma MC, Zhao S, Si W, Li H, Li Y, Deng H, Zhong X. Design and optical characterization of compound eye type solar concentrator. *Res Optic*. 2022;6:Article 100202.
58. Gibson GM, Johnson SD, Padgett MJ. Single-pixel imaging 12 years on: A review. *Opt Express*. 2020;28(19):28190–28208.
59. Abiodun OI, Jantan A, Omolara AE, Dada KV, Mohamed NA, Arshad H. State-of-the-art in artificial neural network applications: A survey. *Heliyon*. 2018;4(11):e00938.
60. Govorov AO, Richardson HH. Generating heat with metal nanoparticles. *Nano Today*. 2007;2(1):30–38.
61. Hornyak GL, Patrissi CJ, Martin CR. Fabrication, characterization, and optical properties of gold nanoparticle/porous alumina composites: The nonscattering Maxwell–Garnett limit. *J Phys Chem B*. 1997;101(9):1548–1555.
62. Adamson AW. An adsorption model for contact angle and spreading. *J Colloid Interface Sci*. 1968;27(2):180–187.
63. Adamson AW. Potential distortion model for contact angle and spreading. II. Temperature dependent effects. *J Colloid Interface Sci*. 1973;44(2):273–281.

64. Wei S, Liu J, Zhao Y, Zhang T, Zheng M, Jin F, Dong X, Xing J, Duan X. Protein-based 3D microstructures with controllable morphology and pH-responsive properties. *ACS Appl Mater Interfaces*. 2017;9(48):42247–42257.
65. Lay CL, Lee MR, Lee HK, Phang IY, Ling XY. Transformative two-dimensional array configurations by geometrical shape-shifting protein microstructures. *ACS Nano*. 2015;9(10):9708–9717.
66. Chan BP, Ma JN, Xu JY, Li CW, Cheng JP, Cheng SH. Femtosecond laser-based free writing of 3D protein microstructures and micropatterns with sub-micrometer features: A study on voxels, porosity, and cytocompatibility. *Adv Funct Mater*. 2014;24(3):277–294.
67. Ritschdorff ET, Nielson R, Shear JB. Multi-focal multiphoton lithography. *Lab Chip*. 2012;12(5):867–871.
68. Huang S, Wang L, Zheng Y, Su Y, Wang F. A simple process optimization route to fabricate curved bionic compound eye array. In: *IOP conference series: Materials science and engineering*. Hangzhou (China): IOP Publishing; 18-20 April 2020. p. 012099.
69. Li J, Wang W, Mei X, Hou D, Pan A, Liu B, Cui J. Fabrication of artificial compound eye with controllable field of view and improved imaging. *ACS Appl Mater Interfaces*. 2020;12(7):8870–8878.
70. Gattass RR, Mazur E. Femtosecond laser micromachining in transparent materials. *Nat Photonics*. 2008;2(4):219–225.
71. Zhu L, Gao Y, Hu X, Ma Z, Zhang W. Progress in femtosecond laser fabrication of artificial compound eye. *Chin Sci Bull*. 2019;64(12):1254–1267.
72. Cao JJ, Hou ZS, Tian ZN, Hua JG, Zhang YL, Chen QD. Bioinspired zoom compound eyes enable variable-focus imaging. *ACS Appl Mater Interfaces*. 2020;12(9):10107–10117.
73. Yamada K, Asano T, Tanida J, Shougenji R, Nagakura T. Development of three dimensional endoscope by compound optics. In: *European conference on biomedical optics*. Munich (Germany): Optica Publishing Group; 2005. p SuD5.
74. Kagawa K, Shogenji R, Tanaka E, Yamada K, Kawahito S, Tanida J. Variable field-of-view visible and near-infrared polarization compound-eye endoscope. Paper presented at: 2012 Annual International Conference of the IEEE Engineering in Medicine and Biology Society; 2012 Aug 28–Sep 1; San Diego, CA, USA.
75. Kagawa K, Tanaka E, Yamada K, Kawahito S, Tanida J. Deep-focus compound-eye camera with polarization filters for 3D endoscopes. Paper presented at: Three-Dimensional and Multidimensional Microscopy: Image Acquisition and Processing XIX; 2012 Feb 2; San Francisco, CA, USA.
76. Kagawa K. A compact shape-measurement module based on a thin compound-eye camera with multiwavelength diffractive pattern projection for intraoral diagnosis. Paper presented at: Optics and Photonics for Information Processing III; 2009 Sep 1; San Diego, CA, USA.
77. Kim K, Jang KW, Kim HK, Bean Cho S, Jeong KH. Biologically inspired intraoral camera for multifunctional dental imaging. *J Optic Microsyst*. 2022;2(3):031202–031202.
78. Kagawa K, Tanabe H, Ogata C, Ogura Y, Nakao Y, Toyoda T, Masaki Y, Ueda M, Tanida J. An active intraoral shape measurement scheme using a compact compound-eye camera with integrated pattern projectors. *Jpn J Appl Phys*. 2009;48(9S2):09LB04.
79. Voelkel R, Herzig HP, Nussbaum P, Daendliker R, Hugle WB. Microlens array imaging system for photolithography. *Opt Eng*. 1996;35(11):3323–3330.
80. Leitel R, Brückner A, Buß W, Viollet S, Pericet-Camara R, Mallot H, Bräuer A. Curved artificial compound-eyes for autonomous navigation, Paper presented at: Micro-Optics 2014; 2014 May 2; Brussels, Belgium.
81. Yoo H, Cha G, Oh S. Deep ego-motion classifiers for compound eye cameras. *Sensors*. 2019;19(23):5275.
82. Pang K, Fang F, Song L, Zhang Y, Zhang H. Bionic compound eye for 3D motion detection using an optical freeform surface. *JOSA B*. 2017;34(5):B28–B35.
83. Zufferey JC, Beyeler A, Floreano D. Autonomous flight at low altitude using light sensors and little computational power. *Int J Micro Air Vehicles*. 2010;2(2):107–117.
84. Beyeler A, Zufferey JC, Floreano D. Vision-based control of near-obstacle flight. *Auton Robot*. 2009;27(3):201–219.
85. Dahmen H, Mallot HA. Odometry for ground moving agents by optic flow recorded with optical mouse chips. *Sensors*. 2014;14(11):21045–21064.
86. Greiner B, Ribi WA, Warrant EJ. Retinal and optical adaptations for nocturnal vision in the halictid bee *Megalopta genalis*. *Cell Tissue Res*. 2004;316:377–390.
87. Laughlin S, Horridge GA. Angular sensitivity of the retinula cells of dark-adapted worker bee. *Z Vgl Physiol*. 1971;74(3):329–335.
88. Wang J, Zhou W, Liu Y, He G, Yang Y. Biomimetic compound eyes with gradient ommatidium arrays. *ACS Appl Mater Interfaces*. 2023;15(37):44503–44512.
89. Hu X, Zhu J, Hu Q, Zheng J, Yang D, Zhou F, Cheng Y, Yang Y. Digital optofluidic compound eyes with natural structures and zooming capability for large-area fluorescence sensing. *Biosens Bioelectron*. 2022;195:Article 113670.
90. Li C, Jiang H. Electrowetting-driven variable-focus microlens on flexible surfaces. *Appl Phys Lett*. 2012;100(23): 231105–2311054.
91. Pohl HA. *Dielectrophoresis: The behabior of neutral matter in nonuniform electric fields*. New York (NY): Stony Brook Foundation Inc.; 1978.
92. Jin B, Ren H, Choi WK. Dielectric liquid lens with chevron-patterned electrode. *Opt Express*. 2017;25(26):32411–32419.
93. Pouydebasque A. Process optimization and performance analysis of an electrostatically actuated varifocal liquid lens. Paper presented at: 2011 16th International Solid-State Sensors, Actuators and Microsystems Conference; 2011 Jun 5–9; Beijing, China.
94. Li H, Ren W, Yang L, Ma C, Tang S, Yuan R. Tunable-focus liquid lens actuated by a novel piezoelectric motor. *Proc Inst Mech Eng C J Mech Eng Sci*. 2021;235(19):4337–4347.
95. Zhang W, Aljasem K, Zappe H, Seifert A. Completely integrated, thermo-pneumatically tunable microlens. *Opt Express*. 2011;19(3):2347–2362.
96. Xu S, Ren H, Lin YJ, Moharam MJ, Wu ST, Tabiryan N. Adaptive liquid lens actuated by photo-polymer. *Opt Express*. 2009;17(20):17590–17595.
97. Jarosz J, Molliex N, Chenon G, Berge B. Adaptive eyeglasses for presbyopia correction: An original variable-focus technology. *Opt Express*. 2019;27(8):10533–10552.
98. Liu C, Wang D, Wang QH. Variable aperture with graded attenuation combined with adjustable focal length lens. *Opt Express*. 2019;27(10):14075–14084.
99. Xia JP, Zhang XT, Sun HX, Yuan SQ, Qian J, Ge Y. Broadband tunable acoustic asymmetric focusing lens from dual-layer metasurfaces. *Phys Rev Appli*. 2018;10(1): Article 014016.

100. Hasan N, Kim H, Mastrangelo CH. Large aperture tunable-focus liquid lens using shape memory alloy spring. *Opt Express*. 2016;24(12):13334–13342.
101. Mao X, Lin SCS, Lapsley MI, Shi J, Juluri BK, Huang TJ. Tunable liquid gradient refractive index (L-GRIN) lens with two degrees of freedom. *Lab Chip*. 2009;9(14):2050–2058.
102. Yang Y, Chin L, Tsai J, Tsai D, Zheludev N, Liu A. Transformation optofluidics for large-angle light bending and tuning. *Lab Chip*. 2012;12(19):3785–3790.
103. Liu H, Shi Y, Liang L, Li L, Guo S, Yin L, Yang Y. A liquid thermal gradient refractive index lens and using it to trap single living cell in flowing environments. *Lab Chip*. 2017;17(7):1280–1286.
104. Wolfe DB, Vezenov DV, Mayers BT, Whitesides GM, Conroy RS, Prentiss MG. Diffusion-controlled optical elements for optofluidics. *Appl Phys Lett*. 2005;87(18):181105.
105. Yang Y, Liu AQ, Chin LK, Zhang XM, Tsai DP, Lin CL, Lu C, Wang GP, Zheludev NI. Optofluidic waveguide as a transformation optics device for lightwave bending and manipulation. *Nat Commun*. 2012;3(1):651.
106. Tang SK, Mayers BT, Vezenov DV, Whitesides GM. Optical waveguiding using thermal gradients across homogeneous liquids in microfluidic channels. *Appl Phys Lett*. 2006;88(6):061112.
107. Chen Q, Jian A, Li Z, Zhang X. Optofluidic tunable lenses using laser-induced thermal gradient. *Lab Chip*. 2016;16(1):104–111.
108. Chen Q, Li T, Li Z, Long J, Zhang X. Optofluidic tunable lenses for in-plane light manipulation. *Micromachines*. 2018;9(3):97.
109. Tuli S, Tuli S, Wander G, Wander P, Gill SS, Dustdar S, Sakellariou R, Rana O. Next generation technologies for smart healthcare: Challenges, vision, model, trends and future directions. *Int Technol Lett*. 2020;3(2):Article e145.
110. Boutteau R, Rossi R, Qin L, Merriaux P, Savatier X. A vision-based system for robot localization in large industrial environments. *J Intell Robot Syst*. 2020;99:359–370.
111. Al Said N, Gorbachev Y, Avdeenko A. An unmanned aerial vehicles navigation system on the basis of pattern recognition applications—Review of implementation options and prospects for development. *Softw Prac Exper*. 2021;51(7):1509–1517.